

# Crystalline chiral condensates off the tricritical point in a generalized Ginzburg-Landau approach

Hiroaki Abuki,<sup>1,\*</sup> Daisuke Ishibashi,<sup>2,†</sup> and Katsuhiko Suzuki<sup>1,‡</sup>

<sup>1</sup>*Department of Physics, Tokyo University of Science,  
Kagurazaka 1-3, Shinjuku, Tokyo 162-8601, Japan*

<sup>2</sup>*Bureau of Waterworks, Tokyo Metropolitan Government,  
Hongo 2-7-1, Bunkyo-ku, Tokyo 163-8001, Japan*

We present an extensive study on inhomogeneous chiral condensates in QCD at finite density in the chiral limit using a generalized Ginzburg-Landau (GL) approach. Performing analyses on higher harmonics of one-dimensionally (1D) modulated condensates, we numerically confirm the previous claim that the solitonic chiral condensate characterized by Jacobi's elliptic function is the most favorable structure in 1D modulations. We then investigate the possibility of realization of several multidimensional modulations within the same framework. We also study the phase structure far away from the tricritical point by extending the GL functional expanded up to the eighth order in the order parameter and its spatial derivative. On the same basis, we explore a new regime in the extended GL parameter space and find that the Lifshitz point is the point where five critical lines meet at once. In particular, the existence of an intriguing triple point is demonstrated, and its trajectory consists of one of those critical lines.

PACS numbers: 12.38.Mh, 21.65.Qr, 25.75.Nq

Keywords: QCD, chiral condensate, quark matter, inhomogeneous phases, crystal structures

## I. INTRODUCTION

How matter behaves as a whole under extreme conditions, such as high temperature and/or density is one of the central questions in hadron physics that, in principle, should be answered by quantum chromodynamics (QCD). At high temperature QCD unambiguously predicts a new, extreme form of matter called the quark-gluon plasma, and its properties are now under extensive investigation from both theoretical and experimental sides, the latter facilitated by heavy ion colliding facilities such as RHIC and the LHC. On the theoretical side, the most powerful tool to investigate this region is the lattice QCD simulations which makes possible *ab initio* calculation of thermodynamic quantities at high temperature.

On the other hand, at finite density lattice simulations still remain less predictive because of a serious problem due to the complex fermion determinant. Our knowledge of the forms of matter at finite density is limited except for ultimately a high density regime where we know, from perturbative QCD computations, matter forms a color superconductor of the color-flavor locked type. Even though the form of matter at accessible density is still obscure, we might expect to have two kinds of phase transition (or crossover) when ordinary nuclei is compressed by an external gravitational pressure: One is the deconfinement [1] and the other is the chiral restoration [2] which is the main topic of this paper.

QCD vacuum is considered as a sea of the chiral condensate [3], namely,  $\bar{q}q$  condensate which may arise due to a strong correlation between a quark and antiquark. The assumption has proven to be useful for interpretation of hadron spectroscopy as well as hadron scatterings at low energy, yet it is only recently that its formation in vacuum was directly checked by lattice simulations of QCD [4]. When the baryon chemical potential is introduced, it breaks the charge conjugation symmetry, bringing an imbalance, i.e., a net excess of quarks over antiquarks. Thus it is possible for the chiral condensate to be broken by such imbalance. In the model calculation this actually takes place through the suppression of  $\bar{q}q$  formation by the Pauli blocking [2, 5].

How the entire chiral restoration takes place is, however, still under the veil. Most of the Nambu–Jona-Lasinio (NJL)-type models predict the first-order phase transition. But it is possible that this transition proceeds hierarchically via several intermediate steps, such as meson condensates. In particular, possibilities of inhomogeneous chiral condensate [chiral density waves (CDW)] have been attracting a lot of interest recently [6–10]. So far proposed CDWs can be classified into two major groups: one is the Flude-Ferrell (FF)-type [11] and the other is the Larkin-Ovchinnikov (LO) type [12]. CDWs in the former group are characterized by some anisotropic pairing in momentum space, while those in the latter group are described by a characteristic modulation in real space.

CDWs can be regarded as femtoscale phase separations as a consequence of the competition between the chiral condensate  $\sigma = \langle \bar{q}q \rangle$  and quark chemical potential  $\mu$ ; the latter drives a stress that promotes the population of quarks,  $n = \langle q^\dagger q \rangle$ , that is, an imbalance in the sea of quark-antiquark condensate. In the case of the FF-type

---

\* h.abuki@rs.tus.ac.jp

† d.ishibashi.1@gmail.com

‡ katsu\_s@rs.tus.ac.jp

CDWs, quarks as impurities are accumulated in some favorable directions on the Fermi surface where the pairing is absent, while in the LO-type CDWs the condensate modulates in real space, taking nodes where quarks are populated without any friction [13]. In a nutshell, it can be said that the CDW is a *halfway* state produced by a compromise between two conflicting effects: the  $\bar{q}q$  condensate and the quark occupation  $q^\dagger q$ .

Essentially the same picture applies to conventional FFLO superconductors in condensed matter physics [11, 12]. It was recently reported that a kind of such exotic superconductors was observed experimentally in 2D films of a heavy fermion compound, CeCoIn<sub>5</sub> [14]. In these systems, an external magnetic field  $h$  drives the Pauli's paramagnetism via yielding a mismatch in the Fermi momenta of two species, in this case, spin up and down. This paramagnetic stress competes with the spin singlet pairing, and as a consequence, the FFLO state may appear as a halfway state between a complete paramagnetic state and a uniform pairing state; when  $h$  exceeds some critical value, the spin density  $n_3(\mathbf{x}) = \langle f^\dagger \tau_3 f \rangle = n_\uparrow(\mathbf{x}) - n_\downarrow(\mathbf{x})$  starts to accumulate near the points where spin singlet pair density  $\Delta(\mathbf{x}) = \langle f^T (i\tau_2) f \rangle = \langle \uparrow\downarrow - \downarrow\uparrow \rangle$  takes nodes in the real (or momentum) space.

Possible formation of inhomogeneous condensates has been discussed in various contexts of high energy physics. These include neutral pion condensates [15], charged pion condensates [16], color superconductors [17–21], chiral magnetic spiral in a strong magnetic field [22], crystal phases in (1 + 1)-dimensional QCD in the large  $N_c$  limit [23], and spiral phases in the quarkyonic phase [24–26]. Inhomogeneous chiral condensates have also been studied extensively in the Gross-Neveu (GN) model with a discrete chiral symmetry [27–31] and also in the corresponding model with a continuous chiral symmetry, i.e. the (1 + 1)-dimensional NJL model in the large  $N$  limit [32].

Even if the crystal structure is restricted to 1D modulations, its impact in the QCD phase diagram is drastic as demonstrated in [10]; it was shown that there is a domain in the phase diagram where the chiral condensate develops a crystallization in a solitonic form characterized by the elliptic function. Accordingly, the tricritical point turns into the Lifshitz point where three phases, a symmetric (Wigner) phase, an inhomogeneous phase, and a homogeneous symmetry-broken phase, meet at once. The analyses were based on the Ginzburg-Landau (GL) functional expanded in the chiral order parameter and its spatial derivatives up to sixth order, which offers a minimal model-independent description of the QCD tricritical point in the chiral limit [33]. Despite the development in understanding the 1D modulated chiral condensate, only a few works have been devoted to exploring multidimensional modulations [26, 34].

The aim of the present paper is twofold: first to seek the most favorable crystallization pattern and, second, to explore the phase structure away from the tricritical point. In connection with the first point, we note that

even in the GL framework it is not so evident that the solitonic chiral crystal characterized by Jacobi's elliptic function gives the absolute ground state. What is shown is that it certainly constitutes a sufficient, particular solution at sixth order of the GL functional. We thus examine other crystal structures as candidates of the ground state, including the possibility of multidimensional crystal structures. For a 1D structure, we search for the most favorable structure taking the most general *Ansatz*, the condensate expanded in the harmonic series [21, 35]. As for a higher dimensional structure, we only examine several specific *Ansätze*.

In order to accomplish the second purpose, we extend the existing GL functional up to eighth order in the condensate and its spatial derivative. This is because the GL functional at sixth order provides us with a minimal description of the critical point, where it follows from a simple scaling rule that the phase structure stays the same even if the region close to the critical point is zoomed out. Moreover there is one more positive reasoning for this extension: It was shown in the context of a superconductor under an external magnetic field that such higher order terms should be taken care to correctly describe phases off the tricritical point [36]. Starting from the BCS model and making use of a quasi-classical (Eilenberger) approximation to the Bogoliubov-de Gennes equation, they numerically found that another type of FFLO phase named FFLO-II shows up in the phase diagram; it replaces a large part of the inhomogeneous phase, which brings a new critical end point located off the tricritical point. In order to understand their results within the GL framework, one needs to work at least at eighth order as pointed out in the paper.

The paper is organized as follows. Section II is mostly devoted to a review on the GL treatment of inhomogeneous chiral condensates made in [21]. We make physics behind a formation of inhomogeneous condensate transparent. In Sec. III, we examine several *Ansätze* for multidimensional crystal structures, as well as the most general *Ansatz* for 1D modulation. We finally address in Sec. IV the question of how the phase structure expands at large distance from the Lifshitz point by extending the previous GL functional up to eighth order. We summarize the present paper in Sec. V.

## II. GENERALIZED GINZBURG-LANDAU APPROACH ON INHOMOGENEOUS PHASES

Nickel studied the possibility of inhomogeneous chiral phases in QCD using a generalized GL approach [10]. Here we review the framework. In order to describe the phase structure close to the tricritical point, we need to retain up to sixth order in the chiral order parameter in the GL Lagrangian. Following [10], we extend the GL Lagrangian such that the theory allows an inhomogeneous phase.

### A. Generalized Ginzburg-Landau functional

To incorporate the energy gain/loss with respect to space variations of the order parameter, we employ the gradient expansion. A generalized GL functional in the chiral limit up to sixth order in the chiral order parameter and its derivative is given by

$$\begin{aligned} \omega(M(\mathbf{x})) &= \frac{\alpha_2}{2} M(\mathbf{x})^2 + \frac{\alpha_4}{4} M(\mathbf{x})^4 + \frac{\alpha_{4b}}{4} (\nabla M(\mathbf{x}))^2 \\ &+ \frac{\alpha_6}{6} M^6 + \frac{\alpha_{6b}}{6} M^2 (\nabla M)^2 + \frac{\alpha_{6c}}{6} (\Delta M)^2. \end{aligned} \quad (1)$$

Nickel derived, starting from an NJL model, relations among parameters  $\{\alpha_n\}$  up to total derivatives:  $\alpha_{4b} = \alpha_4$ ,  $\alpha_{6b} = 5\alpha_6$  and  $\alpha_{6c} = \alpha_6/2$ . Hereafter, we treat these three parameters  $\{\alpha_2, \alpha_4, \alpha_6\}$  as independent GL couplings. In the NJL model, only quark loops contribute to the GL couplings, which may provide a good description at high density regime. Then the generalized GL functional to this order becomes

$$\begin{aligned} \omega(M(\mathbf{x})) &= \frac{\alpha_2}{2} M(\mathbf{x})^2 + \frac{\alpha_4}{4} (M(\mathbf{x})^4 + (\nabla M)^2) \\ &+ \frac{\alpha_6}{6} (M(\mathbf{x})^6 + 5M^2(\nabla M)^2 + \frac{1}{2}(\Delta M)^2). \end{aligned} \quad (2)$$

We can then analyze the phase structure of quark matter in the GL parameter space spanned by  $\{\alpha_2, \alpha_4, \alpha_6\}$ , which can in principle be mapped onto the phase diagram in the  $(\mu, T)$  space in real QCD.

### B. Dimensional and scaling analysis

Parameter  $\alpha_6$  should always be positive for the thermodynamic stability and it has dimension  $\Lambda^{-2}$  with  $\Lambda$  being some energy scale. Then we use  $\alpha_6$  to specify the unit of energy scale. Moreover we can use  $|\alpha_4|$  to adjust the magnitudes of the fourth- and sixth-order coefficients. To be precise, let us introduce dimensionless variables  $\{\eta_2, \omega, m, \tilde{\mathbf{x}}, \tilde{\nabla}\}$  as follows:

$$\begin{aligned} \alpha_2 &= \eta_2 \left[ \frac{\alpha_4^2}{\alpha_6} \right], \\ \omega &= \tilde{\omega} \left[ \frac{|\alpha_4|^3}{\alpha_6^2} \right], \quad M = m \left[ \frac{|\alpha_4|^{1/2}}{\alpha_6^{1/2}} \right], \\ \mathbf{x} &= \tilde{\mathbf{x}} \left[ \frac{\alpha_6^{1/2}}{|\alpha_4|^{1/2}} \right], \quad \tilde{\nabla} = \nabla_{\tilde{\mathbf{x}}}. \end{aligned} \quad (3)$$

Then, in these dimensionless bases, the GL functional takes the form

$$\begin{aligned} \tilde{\omega} &= \frac{\eta_2}{2} m^2 + \frac{\text{sgn}(\alpha_4)}{4} \left( m^4 + (\tilde{\nabla} m)^2 \right) \\ &+ \frac{1}{6} \left( m^6 + 5m^2(\tilde{\nabla} m)^2 + \frac{1}{2}(\tilde{\Delta} m)^2 \right). \end{aligned} \quad (4)$$

Now we see that the problem has only one continuous parameter  $\eta_2$ . What we have to work out now is to find the phase structure in  $\eta_2$  space both for positive and negative  $\alpha_4$  cases, and then map them back onto the

original GL parameter space  $\{\alpha_2, \alpha_4, \alpha_6\}$  according to the scaling relation between  $\alpha_2$  and  $\eta_2$  in Eq. (3).

In the following we use  $\{\alpha_2, M, \mathbf{x}\}$  instead of  $\{\alpha_2 \alpha_6, M \sqrt{\alpha_6}, \mathbf{x} / \sqrt{\alpha_6}\}$  to avoid notational complications. They should be understood as dimensionless ones measured in the proper units, i.e.,  $[\alpha_6^{-1}]$ ,  $[\alpha_6^{-1/2}]$  and  $[\alpha_6^{1/2}]$ .

### C. Condition for soliton/condensate formation

For  $\alpha_4 > 0$  the phase structure is simple. One has a uniform chiral symmetry-broken phase ( $M \neq 0$ ,  $\chi$ SB phase) for  $\eta_2 < 0$  and symmetry restored phase ( $M = 0$ , Wigner phase) for  $\eta_2 > 0$ , separated by a second-order phase transition. On the other hand, phases for  $\alpha_4 < 0$  are rather rich [10]. When the condensate is restricted to be constant in space, there are only two phases: the  $\chi$ SB phase at small  $\eta_2$  and the Wigner phase at large  $\eta_2$ , separated by a first-order phase transition at  $\eta_2 = 3/16 \equiv \eta_2^c$ . Once the chiral condensate is allowed to have variations in space, the first-order phase transition splits into two second-order phase transitions, one at  $\eta_2^I = 5/36 < \eta_2^c$ , the other at  $\eta_2^{II} = 3/8 > \eta_2^c$ , and in between an inhomogeneous phase shows up [10] as we will discuss below.

Let us start with a one-dimensional sinusoidal chiral density wave [6, 7] (the LO state) characterized by

$$M_{\text{LO}}(\mathbf{x}) = \sqrt{2} M_{\text{II}} \sin(k_{\text{II}} z). \quad (5)$$

Averaging the GL free energy density over the Wigner-Seitz cell, optimizing the wave vector  $k_{\text{II}}$  with respect to  $M_{\text{II}}$ , and finally expanding the GL free energy in  $M_{\text{II}}$ , we obtain for  $\alpha_4 < 0$ , up to quartic order in  $M_{\text{II}}$ ,

$$\begin{aligned} \Omega &= \langle \omega(M_{\text{LO}}(\mathbf{x})) \rangle_{\text{WS}} \\ &= \left( \frac{\eta_2}{2} - \frac{3}{16} \right) M_{\text{II}}^2 + \frac{1}{4} M_{\text{II}}^4 + \mathcal{O}(M_{\text{II}}^6). \end{aligned} \quad (6)$$

From this, it is clear that the system undergoes a second-order transition from the Wigner phase to the LO state when the parameter  $\eta_2$  crosses  $\eta_2^{II} = 3/8$  from above.

Now we move on to the region of the lower value of  $\eta_2$ , where the chiral symmetry is broken by a homogeneous condensate. Consider the situation where a single soliton (a kink in 1D [27, 30, 31], actually a domain wall in 3D [10]) is formed in a sea of homogeneous condensate. When  $\eta_2$  is small, there is an energy cost for the creation of such a kink in the homogeneous condensate. However, this energy cost decreases with increasing  $\eta_2$ , and at some critical point which we denote by  $\eta_2^I$  it vanishes. To see this, we first set an *Ansatz* for the domain wall profile as

$$M_{\text{SS}}(z) = M_{\text{I}} \tanh(k_{\text{I}} z), \quad (7)$$

where  $M_{\text{I}}$  is the homogeneous condensate, being a function of  $\eta_2$ . The energy cost accumulated within the domain wall surface per unit area can be defined by

$$\ell \Omega_{\ell}(M_{\text{I}}, k_{\text{I}}; \eta_2) \equiv \int_{-\ell/2}^{\ell/2} dz (\omega(M_{\text{SS}}(z)) - \omega(M_{\text{I}})). \quad (8)$$

where  $\ell$  is the system length in the  $z$  direction which will be taken to be infinity. Optimizing the value of  $k_I$  requiring that the energy cost  $F(\eta_2, k_I) = \lim_{\ell \rightarrow \infty} [\ell \delta \Omega_\ell(M_I, k_I; \eta_2)]$  takes minimum, we obtain the relation  $k_I = M_I$ . The function  $f(\eta_2) \equiv F(\eta_2, M_I(\eta_2))$  is depicted in Fig. 1(a), from which we see that it is a monotonically decreasing function of  $\eta_2$ , and at the critical point which we denote by  $\eta_2^I$  it crosses zero. At this point, a soliton will be formed spontaneously without any energy cost. It is easy to derive  $\eta_2^I = 5/36$  where  $M_I = \sqrt{5/6}$ , and in fact  $f(\eta_2)$  is expanded in powers of  $\Delta \equiv (\eta_2 - 5/36)$ , as  $f(\eta_2) = -\frac{5}{6}\Delta + \frac{9}{8}\Delta^2 + \mathcal{O}(\Delta^3)$ . In the figure, we denote by a solid circle  $\eta_2^c = 3/16$ , and by the cross  $\eta_2^{II} = 2\eta_2^c$  for comparison. Obviously the domain wall formation is faster to take place than the first-order phase transition to the Wigner phase when  $\eta_2$  is increased. We conclude that some kind of inhomogeneous phase should develop in the window  $\eta_2^I < \eta_2 < \eta_2^{II}$ .

In order to elucidate on what drives the formation of a domain wall in the spatially uniform  $\chi$ SB phase at the critical point  $\eta_2^I$ , we show in Fig. 1(b) the energy density profile of a single soliton by the bold line. The spatial profile of the soliton is also shown by the thin line. Several contributions to the energy density are shown separately: The dotted (red) line shows the energy loss through the homogeneous parts in the GL functional, while the dashed (blue) and dot-dashed (green) lines show the contribution from the derivative terms at the fourth and sixth orders, respectively. We confirm that the derivative term at the fourth order is responsible for the formation of a kink in the chiral condensate.

#### D. Solitonic solution at sixth order of GL expansion

We have seen that, for  $\alpha_4 < 0$ , the first-order chiral restoration at  $\alpha_2 = \eta_2^c \alpha_4^2 / \alpha_6$  is replaced by two second-order critical lines, one at  $\alpha_2 = \eta_2^I \alpha_4^2 / \alpha_6$  representing the onset of the formation of a single soliton in a homogeneous sea of chiral condensate, and the other at  $\alpha_2 = \eta_2^{II} \alpha_4^2 / \alpha_6$ , corresponding to the chiral restoration from an inhomogeneous chiral phase. In short, the chiral restoration becomes a smooth, hierarchical two-step transition. So now the question is how does the system develop from a single soliton state to a sinusoidal LO-type state as  $\eta_2$  is increased from  $\eta_2^I$  to  $\eta_2^{II}$ ? This was already addressed in the paper [31, 37, 38] where it is shown that the solution which covers these two situations is the solitonic condensate characterized by Jacobi's elliptic function. Here we closely follow the discussion in [37] and demonstrate that, if the modulation is restricted to 1D, Jacobi's elliptic function gives in fact an adequate solution to the problem. Let us start with the Euler-Lagrange (EL) equation for the inhomogeneous chiral condensate,

$$\frac{\delta}{\delta M(\mathbf{x})} \int_{\text{WS}} d\mathbf{y} \omega(M(\mathbf{y})) = 0.$$

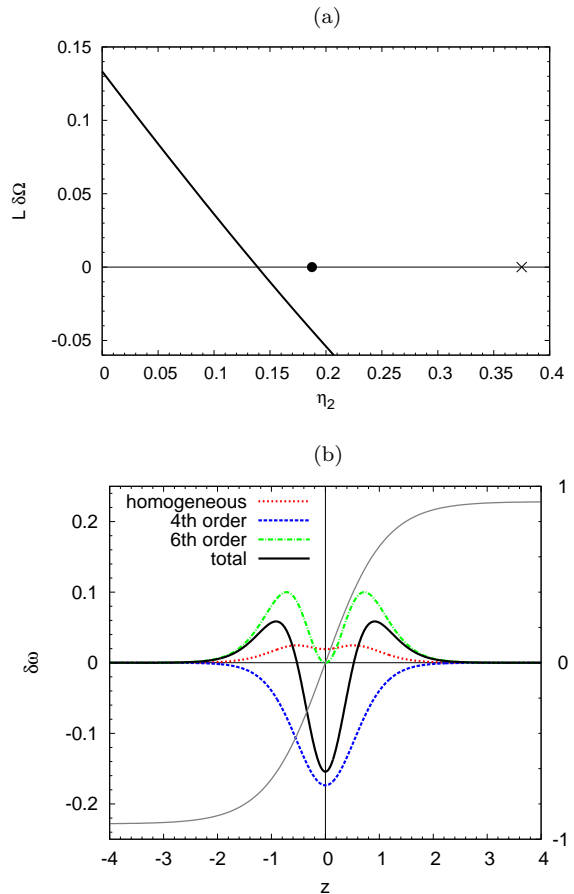


FIG. 1. (color online). (a) Energy per unit area required for the creation of a single soliton as a function of  $\eta_2$ . The solid circle and the cross placed on the  $\eta_2$  axis represent points  $\eta_2 = \eta_2^I$  and  $\eta_2 = \eta_2^c$ . See text for details. (b) A single soliton profile  $M_{\text{SS}} = M_I \tanh(M_I z)$  with  $M_I = \sqrt{5/6}$  being the mass at  $\eta_2 = \eta_2^I$  and the associated energy density profile. Contributions from homogeneous parts, and those from derivative terms (at the fourth and sixth orders separately), are also shown.

The condition results in the following fourth-order ordinary, but nonlinear differential equation (when  $\alpha_4 < 0$ ):

$$0 = M^{(4)}(z) + 3M'' - 10 [M(M')^2 + M^2 M''] + 6\eta_2 M - 6M^3 + 6M^5. \quad (9)$$

We need to solve this equation to find a suitable 1D modulation. There is no systematic way to find out the general solution to a fourth-order nonlinear differential equation. However it is not so difficult to see that Jacobi's elliptic function is a particular solution to Eq. (9) [37]. Let  $\text{sn}(z, \nu)$  be Jacobi's elliptic function with  $\nu$  being the elliptic modulus. We then set

$$M_{\text{sn}}(z) = M_0 \nu \text{sn}(kz, \nu), \quad (10)$$



where  $k$  and  $M_0$  are constants<sup>1</sup>. Following the discussion in [37], we can show that this function obeys a fourth-order differential equation

$$\begin{aligned}
0 = & M_{\text{sn}}^{(4)} + (A+1)k^2(\nu^2+1)M_{\text{sn}}'' \\
& - \frac{k^2}{M_0^2}(12-B)[M_{\text{sn}}(M_{\text{sn}}')^2 + M_{\text{sn}}^2 M_{\text{sn}}''] \\
& + [Ak^4(\nu^2+1)^2 - B\nu^2]M_{\text{sn}} \\
& - \frac{2k^4}{M_0^2}(1+\nu^2)(3-B+A)M_{\text{sn}}^3 + \frac{3k^4}{M_0^4}(4-B)M_{\text{sn}}^5,
\end{aligned} \tag{11}$$

with  $A$  and  $B$  being arbitrary numbers. Comparing Eq. (10) and Eq. (11), we see that  $M_{\text{sn}}$  constitutes a sufficient solution to the EL equation (10) when the following five algebraic equations are all satisfied:

$$6\eta_2 = k^4 [A(\nu^2+1)^2 - B\nu^2], \tag{12a}$$

$$-3 = -(1+A)k^2(\nu^2+1), \tag{12b}$$

$$10 = \frac{k^2}{M_0^2}(12-B), \tag{12c}$$

$$-6 = -\frac{2k^4}{M_0^2}(1+\nu^2)(3-B+A), \tag{12d}$$

$$6 = \frac{3k^4}{M_0^4}(4-B). \tag{12e}$$

From Eqs. (12c) and (12e), we see  $(M_0/k, B) = (1, 2)$  or  $(M_0/k, B) = (2, -28)$ , but the latter results in complex  $k^2$  and  $\nu$ . Then we take the choice  $(M_0/k, B) = (1, 2)$ , and in this case we see Eqs. (12b) and (12d) are degenerate so that we are left with only two algebraic equations (12a) and (12b), whereas we still have three unknown parameters,  $\nu$ ,  $k$ , and  $A$ . From these two equations we can solve  $\nu$  and  $k$  as a function of the continuous parameter  $A$  (and  $\eta_2$ ). Denoting these functions as  $k_A$  and  $\nu_A$ , we arrive at a one-parameter solution group to the EL equation:

$$M_{\text{sn}}(z; A) = k_A \nu_A \text{sn}(k_A z, \nu_A). \tag{13}$$

We stress that for any value of  $A$ , as long as  $0 \leq \nu_A \leq 1$  and  $k_A^2 > 0$  are both satisfied,  $M_{\text{sn}}(z; A)$  gives a solution to the EL equation. The potential  $\Omega(M_{\text{sn}}(z; A))$  depends on  $A$  so that we need to look for an optimized value of  $A$  demanding that it takes a minimum. This is easy to work out numerically for  $\eta_2^{\text{I}} \leq \eta_2 \leq \eta_2^{\text{II}}$ . We see  $A \rightarrow 4/5$  as  $\eta_2 \rightarrow \eta_2^{\text{I}} + 0$ , where  $\nu_A$  approaches unity ( $\nu_A \rightarrow 1$ ) and  $k_A \rightarrow k_{\text{I}} = \sqrt{5/6}$ ,

$$\lim_{\eta_2 \rightarrow \eta_2^{\text{I}} + 0} M_{\text{sn}}(z; A) = k_{\text{I}} \tanh(k_{\text{I}} x), \tag{14}$$

while  $A \rightarrow 1$  as the other end  $\eta_2 = \eta_2^{\text{II}} - 0$  is approached, where  $\nu_A$  goes vanishing and  $k_A \rightarrow k_{\text{II}} \equiv \sqrt{3/2}$ ,

$$\lim_{\eta_2 \rightarrow \eta_2^{\text{II}} - 0} M_{\text{sn}}(z; A)/\nu_A = k_{\text{II}} \sin(k_{\text{II}} x). \tag{15}$$

<sup>1</sup> In Ref. [10], rather  $\nu_2 = \nu^2$  is treated as an argument of Jacobi's elliptic function. In this notation Eq. (10) becomes  $M_0 \sqrt{\nu_2} \text{sn}(kz, \nu_2)$ .

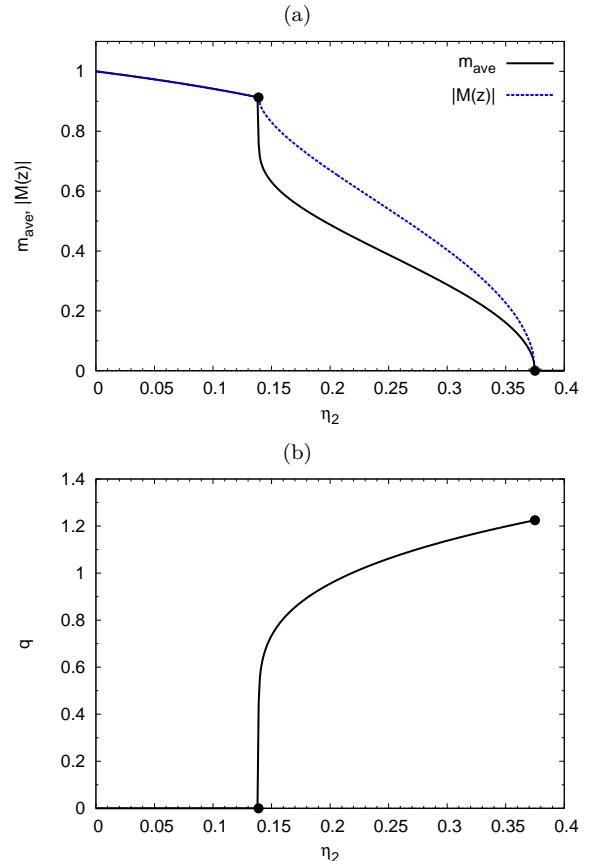


FIG. 2. (color online). **(a)** The amplitude of the dynamical mass and an effective order parameter  $m_{\text{ave}}$  in the solitonic phase as a function of  $\eta_2$ . **(b)** The magnitude of wave vector  $q = 2\pi/\ell_{\text{P}}$  as a function of  $\eta_2$  in the solitonic phase.

In the latter limit,  $\nu_A$  goes zero so that the magnitude of condensate  $|M(z)|$  vanishes while its form becomes sinusoidal. These two limits are given by exactly the same forms as we assumed in the previous section. We show in Fig. 2(a) the amplitude of mass function  $\nu_A k_A$  as a function of  $\eta_2$ . Also depicted together is an effective order parameter  $m_{\text{ave}}$  defined by the root-mean-square mass averaged over the elliptic modulation period  $\ell_{\text{P}} = 4K(\nu_A)/k_A$  with  $K$  being the complete elliptic integral of the first kind:

$$m_{\text{ave}} = \sqrt{\langle M(z)^2 \rangle} = k_A \sqrt{1 - E(\nu_A)/K(\nu_A)}. \tag{16}$$

$E$  is the complete elliptic integral of the second kind. We also show in Fig. 2(b) the magnitude of wave vector  $q = 2\pi/\ell_{\text{P}}$ . From these figures, we clearly see that both phase transitions at  $\eta_2^{\text{I}}$  and  $\eta_2^{\text{II}}$  are continuous ones.

Finally we show in Fig. 3 the phase diagram in the  $[\alpha_2, \text{sgn}(\alpha_4)\alpha_4^2]$  plane which is essentially the same as the one displayed in figure 1 of Ref. [10].

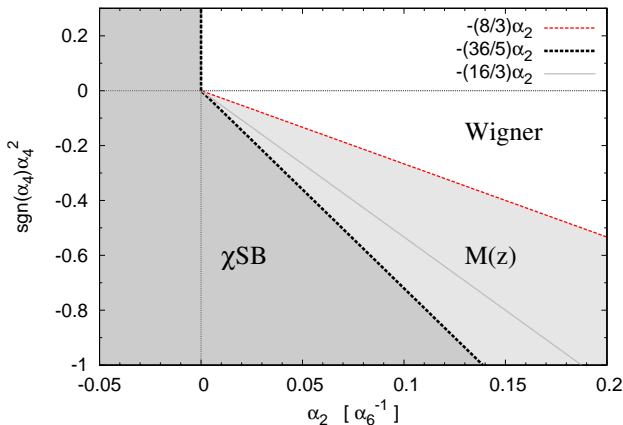


FIG. 3. (color online). The phase diagram in the  $[\alpha_2, \text{sgn}(\alpha_4)\alpha_4^2]$  plane. The horizontal axis represents  $\alpha_2$  measured in the unit  $[\alpha_6^{-1}]$ , namely  $\alpha_2\alpha_6$ . For  $\alpha_4 \geq 0$ , the  $\chi$ SB phase ( $\alpha_2 < 0$ ) and the Wigner phase ( $\alpha_2 > 0$ ) are separated at  $\alpha_2 = 0$  by a second-order phase transition. For  $\alpha_4 < 0$ , there are three phases: the homogeneous chiral condensate indicated by  $\chi$ SB, the solitonic chiral phase marked by  $M(z)$ , and the Wigner phase. Phase transitions separating these three phases, the dashed lines (black and red), are second order. For comparison, would-be first-order phase transition from the homogeneous  $\chi$ SB phase to the Wigner phase is also shown by the thin solid (gray) line inside the inhomogeneous phase.

### E. Singular behavior of thermodynamic quantities at the onset of soliton formation

The phase transition at  $\eta_2 = \eta_2^{\text{II}}$  from the Wigner phase to the solitonic phase is second order, as clearly seen from the GL potential Eq. (6). What about the order of transition for a soliton formation at  $\eta_2 = \eta_2^{\text{I}}$ ? Near the critical point  $\nu = 1$ , the modulation period diverges logarithmically as  $\ell_P \sim 4K(\nu) \sim -2\log((1-\nu)/8)$  so that the spatial separation between domain walls, a half period  $\ell_P/2$ , also becomes large. The corresponding wave vector  $q = 2\pi/\ell_P = \frac{\pi k}{2K(\nu)}$  behaves as

$$q(\nu \rightarrow 1^-) = -\frac{\pi\sqrt{5/6}}{\log((1-\nu^2)/16)}. \quad (17)$$

We see that the wave vector drops to zero, inversely proportional to the logarithm of  $(1-\nu)$ , just as quark number density in the GN model [28, 29]. The problem is how the elliptic modulus behaves as a function of  $\eta_2$  near the critical point. As  $\eta_2^{\text{I}}$  is approached, we see  $\nu \rightarrow 1$ ,  $k^2 \rightarrow 5/6$  with  $A \rightarrow 4/5$ . From Eqs. (12a) and (12b), we can extract the expansion of  $\nu$  and  $k^2$  in terms of  $(4/5 - A)$  and  $\eta_2 - \eta_2^{\text{I}}$ . To first nontrivial order, we find

$$\begin{aligned} 1 - \nu^2 &= \frac{4}{\sqrt{3}}\sqrt{\left(\frac{4}{5} - A\right) + \frac{81}{25}(\eta_2 - \eta_2^{\text{I}})}, \\ k^2 - \frac{5}{6} &= \frac{5}{3\sqrt{3}}\sqrt{\left(\frac{4}{5} - A\right) + \frac{81}{25}(\eta_2 - \eta_2^{\text{I}})}. \end{aligned} \quad (18)$$

Also the relation between  $A$  and  $\eta_2 - \eta_2^{\text{I}}$  was numerically found to be linear in the vicinity of critical point ( $\eta_2 \gtrsim \eta_2^{\text{I}}$ ), as  $A \cong \frac{4}{5} - 2.406(\eta_2 - \eta_2^{\text{I}})$ . We obtain

$$\begin{aligned} 1 - \nu^2 &= \frac{2}{\sqrt{3}}\kappa_{\text{I}}\sqrt{\eta_2 - \eta_2^{\text{I}}}, \\ k^2 - \frac{5}{6} &= \frac{5}{3\sqrt{3}}\kappa_{\text{I}}\sqrt{\eta_2 - \eta_2^{\text{I}}}, \end{aligned} \quad (19)$$

with a numerical value of  $\kappa_{\text{I}} \cong 2.38$ . Therefore, when the critical point  $\eta_2^{\text{I}}$  is approached from above, the inverse of the modulation length behaves as

$$q(\eta_2 \rightarrow \eta_2^{\text{I}} + 0) \sim -\frac{\pi\sqrt{10/3}}{\log\left(\frac{\kappa_{\text{I}}^2}{48}(\eta_2 - \eta_2^{\text{I}})\right)}. \quad (20)$$

We have checked to see that this analytical formula excellently reproduces the numerical result displayed in Fig. 2(b). This means that the separation of domain walls becomes logarithmically large while the wall thickness (the size of defect  $\sim 1/k$ ) does not change drastically near  $\eta_2^{\text{I}}$ .

We now look at the singular behaviors in the thermodynamic quantities. These are determined by the behavior of derivatives of the GL free energy with respect to the parameter  $\eta_2$ . The first derivative in the vicinity of the critical point can be computed up to the first few orders in the expansion in  $\eta_2$  as

$$\begin{aligned} \frac{\partial\Omega}{\partial\eta_2} &= \frac{1}{2}\langle M(z)^2 \rangle_{\text{WS}} \\ &\cong \begin{cases} \frac{5}{12} - \frac{3}{4}(\eta_2 - \eta_2^{\text{I}}) + \dots, & (\eta_2 < \eta_2^{\text{I}}) \\ \frac{5}{12} + \frac{5}{3\log\left(\frac{\kappa_{\text{I}}^2}{48}(\eta_2 - \eta_2^{\text{I}})\right)} + \dots, & (\eta_2 > \eta_2^{\text{I}}) \end{cases} \end{aligned} \quad (21)$$

We see that the first derivative is continuous. The second derivative is also worked out, and the first two dominant parts (either regular or singular) can be extracted as

$$\frac{\partial^2\Omega}{\partial\eta_2^2} \sim \begin{cases} -\frac{3}{4} - \frac{27}{8}(\eta_2 - \eta_2^{\text{I}}) + \dots, & (\eta_2 < \eta_2^{\text{I}}) \\ -\frac{5 + \frac{5}{3}\kappa_{\text{I}}\sqrt{\eta_2 - \eta_2^{\text{I}}}}{3(\eta_2 - \eta_2^{\text{I}})\log^2\left(\frac{\kappa_{\text{I}}^2}{48}(\eta_2 - \eta_2^{\text{I}})\right)} + \dots, & (\eta_2 > \eta_2^{\text{I}}) \end{cases} \quad (22)$$

It is clear that the second derivative is not only discontinuous but diverges as the critical point is approached from the side of the inhomogeneous phase. The singular behavior is characterized mainly by the power law but with a logarithmic correction just as with the fermion number susceptibility in the GN model [28, 29]. We see that the transition is second order. We remark that the same singularity was obtained also in the NJL model [13] where it was shown further that the vector-type interaction between quarks washes out the singular behavior.

Before closing this section, we briefly discuss the origin of the singular behavior of the second derivative of  $\Omega$ . At  $T = 0$  the singularity is related to that of quark number susceptibility [13, 28, 29]. To see this, we first note that at  $T = 0$  a net quark number (imbalance to  $\bar{q}q$  condensate) tends to accumulate in the wall surfaces where

the magnitude of the chiral condensate vanishes. Then considering the fact that the separation length between domain walls diverges as  $\ell_P/2 \sim 1/\log(\eta_2 - \eta_2^I)$  while the size of the wall where quarks are present,  $1/k$ , stays almost constant, the averaged quark number density may be approximately computed as

$$\langle q^\dagger q \rangle \sim n_0 \frac{1/k}{\ell_P + 1/k} \sim -\frac{n_0}{\log\left(\frac{\kappa_1}{48}(\eta_2 - \eta_2^I)\right)}, \quad (23)$$

with  $n_0$  defined as the quark density in the absence of a condensate. Assuming  $n_0$  does not change significantly in the vicinity of the critical point, the quark number susceptibility on the side of the inhomogeneous phase becomes

$$\frac{d\langle q^\dagger q \rangle}{d\mu} \sim \frac{dn_0}{d\mu} \frac{n_0}{(\eta_2 - \eta_2^I) \left[\log\left(\frac{\kappa_1}{48}(\eta_2 - \eta_2^I)\right)\right]^2}. \quad (24)$$

This has exactly the same parametric dependence on  $\eta_2$  as Eq. (22), suggesting that at  $T = 0$  the divergence of the second derivative of  $\Omega$  has originated in the divergent quark number susceptibility [13, 28, 29].

### III. OTHER CRYSTALLIZATION PATTERNS IN 1D AND HIGHER DIMENSIONAL MODULATIONS

In this section we address the question of whether or not states other than the solitonic condensate, with either 1D or higher dimensional modulations, are possible. We work near the Lifshitz point, so we retain up to sixth order in GL expansion as in the previous section. In Sec. III A, we discuss the thermodynamics of the LO-like chiral condensate, Eq. (5), and the FF-like chiral spiral [9] in some detail. Even though these two states are less favorable than the solitonic solution, the analysis still serves as an illustrative benchmark when we explore higher dimensional modulations. In Sec. III A, we try a general Ansatz for the 1D modulation, i.e., the condensate expanded in higher harmonics. For comparison, we also make a harmonic analysis on the solitonic state. In Sec. III B we introduce higher dimensional analogs of the LO-like chiral density wave, and see if such higher dimensional chiral lattices can be realized near the Lifshitz point.

#### A. Real chiral density wave and chiral spiral

Here we discuss the thermodynamics of two typical chiral density waves: a real, LO-like sinusoidal chiral density wave of the form Eq. (5) and a FF-like chiral spiral characterized by a single plane wave

$$M_{\text{FF}}(z) = M_0 e^{ikz}. \quad (25)$$

The imaginary part should be understood as the pseudoscalar condensate, for one choice in the charge neutral

channel:  $M_{\text{FF}}(\mathbf{x}) \sim -2G(\langle \bar{q}q \rangle + i\langle \bar{q}\gamma_5 i\tau_3 q \rangle)$ . This is also called the ‘‘dual chiral density wave’’ abbreviated to the DCDW in the original paper [9]. In the following we refer to this state mainly as the FF state or chiral spiral. When the chiral condensate involves a finite imaginary part, we need to generalize the GL functional so as to allow it. The generalized functional for complex chiral condensates but with restriction to 1D modulations was worked out first in the chiral GN model [30]; the resulting functional has terms asymmetric with respect to an interchange between the real and imaginary parts of the condensate,  $\text{Re}(m) \leftrightarrow \text{Im}(m)$ . These terms are responsible for the realization of the FF-type complex chiral condensate in the GN model [27] and also in the (1+1)-dimensional NJL model in the large  $N$  limit [16, 32]. In the NJL model in the 1+3 dimension, however, these terms are shown to vanish [10]. Then the functional is cast in the following form in the chiral limit, using the same convention as Eq. (4):

$$\begin{aligned} \tilde{\omega} = & \frac{\eta_2}{2}|m|^2 + \frac{1}{4}\text{sgn}(\alpha_4)(|m|^4 + |m'|^2) \\ & + \frac{1}{6}(|m|^6 + 4|m|^2|m'|^2 + \text{Re}(m')^2(m^*)^2 + \frac{1}{2}|m''|^2). \end{aligned} \quad (26)$$

When the condensate is real [ $m(z)^* = m(z)$ ], this functional reduces to Eq. (4) with the restriction to the 1D modulation,  $M(\mathbf{x}) \rightarrow M(z)$ , substituted. As before, we concentrate on the case  $\alpha_4 < 0$ . In Fig. 4 we show the amplitude of masses (a), the magnitude of wave vectors (b), and corresponding thermodynamic potentials (c) for the FF and LO condensates, as a function of  $\eta_2$ . The wave vector  $q$  is just  $k$  ( $k_{\text{II}}$ ) for the FF (LO) state, while for the solitonic state it is given by  $2\pi/\ell_P$ . From the figures, we see that the real LO phase is more favorable than the FF-like chiral spiral over the whole range of  $\eta_2$ , while they are less favorable than the solitonic phase, which will often be denoted by the solitonic (SN) state hereafter. The FF and LO (and SN) states become degenerate at the onset of condensate at  $\eta_2^{\text{II}} = 3/8$ . Near the point it is easy to perform the expansion in  $M_0$ . The result for the LO phase is already given by Eq. (6), and that for the FF phase is obtained at the same order in  $M_0$  as [10]

$$\begin{aligned} \Omega = & \langle \omega(M_{\text{FF}}(\mathbf{x})) \rangle_{\text{WS}} \\ = & \left(\frac{\eta_2}{2} - \frac{3}{16}\right) M_0^2 + \frac{1}{2} M_0^4 + \mathcal{O}(M_0^6). \end{aligned} \quad (27)$$

The coefficient of  $M_0^4$  for the FF phase is twice as large as that of the LO phase, from which we see that the energy for the FF phase is higher than that for the LO phase at least near the onset. This may be reasonably understood along the same line as [39, 40] where it is stressed that additional terms are required in the effective theory in order to recover the broken time reversal symmetry in the FF state, which results in an extra energy cost.

Since the LO phase is more favorable than the FF phase, we concentrate on the LO phase in the following. The transition between the homogeneous  $\chi$ SB and LO phases is of first order. We can obtain the critical  $\eta_2$  by solving  $\min_M \omega(M_{\text{const.}}) = \min_{M,k} \langle \omega(M_0 \sin kz) \rangle_{\text{WS}}$ .

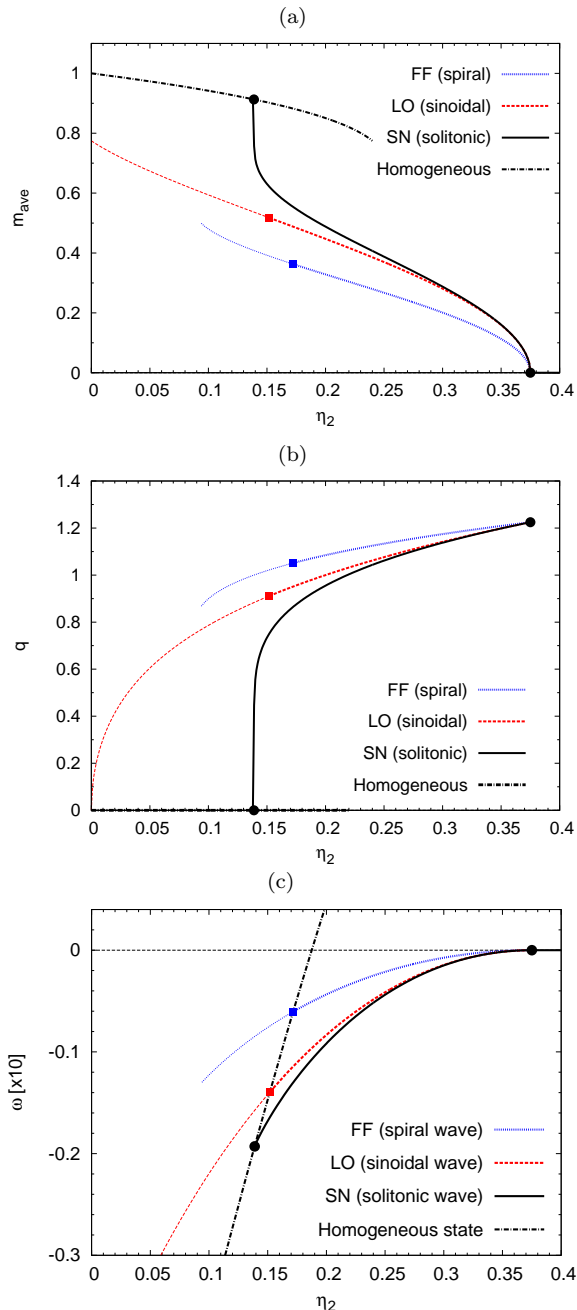


FIG. 4. (color online). (a) Effective order parameters, (b) wave vectors, and (c) potentials as a function of  $\eta_2$  for the LO (dashed, red), FF (dotted, blue) and SN (solid) states. The quantities corresponding to the homogeneous condensate are shown by dot-dashed lines. The solid lines are the same as those depicted in Fig. 2.

This was worked out numerically and the location of the critical point was found as

$$\eta_2(\text{LO} \leftrightarrow \chi\text{SB}) \cong 0.1519, \quad (28)$$

which is larger than  $\eta_2^I \sim 0.1389$  for a soliton formation, reflecting the fact that the LO phase is metastable against the SN phase. Crossing the critical point from

the  $\chi\text{SB}$  phase to the LO phase, the magnitude of the condensate drops by about 20%. Also the ratio of the amplitude of mass to the magnitude of the wave vector in the LO phase just at the critical point has been found to be about 0.8. These can be summarized as

$$\frac{M_0(\text{LO})}{M_{\text{const.}}(\chi\text{SB})} \cong 0.81, \quad \frac{M_0(\text{LO})}{k(\text{LO})} \cong 0.80. \quad (29)$$

We note that all these ratios are the universal constants associated with the first-order phase transition between the  $\chi\text{SB}$  and LO phases, at the sixth order we are working.

We also remark that the first *Ansatz* of counting  $M_0$  and  $k$  as the same order in magnitude is consistent at this transition. At the onset of the condensate, however, the amplitude  $M_0$  vanishes while  $k$  remains finite so that the derivative terms are more important than the bulk homogeneous terms. In contrast, at the onset of the domain wall formation, the derivative terms play a minor role.

## B. Most general condensate with higher harmonics

We here try to see if Jacobi's elliptic function is the most favorable solution among 1D modulation patterns. We first note that Jacobi's elliptic function just gives a one parameter subgroup of solutions to the EL equation. It should be stressed that the original EL equation (9) is a nonlinear fourth-order differential equation while Eq. (11) is basically the sum of three differential equations each of which can be obtained from the second order differential equation which the elliptic function obeys. It is thus not obvious that it really covers all the solutions to the original EL equation. Keeping this in mind, we try the most general assumption for the spatially modulated chiral condensate. We set the condensate in the form of a harmonic expansion series as

$$M_{\text{HH}}(z; \{\ell_{\text{H}}, M_n^{\text{H}}\}) = \sum_{n=1,3,5,\dots} M_n^{\text{H}} \sin((2\pi/\ell_{\text{H}})nz), \quad (30)$$

where  $\{M_n\}$  and  $\ell_{\text{H}}$  are variational parameters. We note that the even components are absent if we restrict the condensate to a half antiperiodic period  $M(z + \ell_{\text{H}}/2) = -M(z)$ . This is quite reasonable for the case of the chiral limit. In fact we have checked numerically that the even components are vanishing even if included. Hereafter, we abbreviate the state characterized by  $M_{\text{HH}}$  as the higher harmonic (HH) state. We took into account up to the fifth harmonics in the expansion above and minimized the thermodynamic potential with respect to  $M_1^{\text{H}}, M_3^{\text{H}}, M_5^{\text{H}}$  and the modulation period  $\ell_{\text{H}}$ .

The resulting energy of the HH state appeared to be very close to that of the SN state. In order to illustrate the fact, we depict in Fig. 5(a) the effective order parameter  $m_{\text{ave}} = \sqrt{M_{\text{HH}}/M_{\text{SN}}(z)^2}$  as a function of  $\eta_2$ , both for the SN and HH states: the solid line for the SN state,



and the dashed (magenta) line for the HH state. We have labeled four representative points,  $\eta_2 = 0.3749, 0.2569, 0.1536,$  and  $0.1389,$  by letters **A**, **B**, **C**, and **D**. In the figure, the coordinate  $(\eta_2, m_{\text{ave}})$  at each point for the SN (HH) state is marked by the lower (upper) triangle. We see that the difference between the HH and SN states is visible only at point **D** which is very close to  $\eta_{\text{I}}$  for the domain wall onset.

The spatial profile of the HH-condensate,  $M_{\text{HH}}(z)$ , was also observed to converge to that of the solitonic state,  $M_{\text{sn}}(z)$ ; the difference is actually invisible already at this level of truncation in the biggest range of  $\eta_2$ . It only becomes slightly manifest in the very vicinity of  $\eta_2 = \eta_2^{\text{I}}$  where the condensate becomes a collection of domain wall solitons. In Figs. 5(b) and (c), we show the spatial profiles of the mass function at points **A**, **C** and **D**. Only at **D** do we show both  $M_{\text{HH}}$  and  $M_{\text{sn}}$ , since at other points the differences are invisible.

In order to see most efficiently how the HH and SN states diverge as the soliton onset is approached, we now make the harmonic analysis on the solitonic condensate  $M_{\text{sn}}$ . First we note that the decomposition of the elliptic function in the Fourier-Lambert series is given as

$$M_{\text{sn}}(z; \{\nu, k\}) = \sum_{n=1,3,\dots}^{\infty} M_n^{\text{sn}}(\nu, k) \sin\left(\frac{2\pi n z}{\ell_{\text{P}}(\nu, k)}\right),$$

$$M_n^{\text{sn}}(\nu, k) = \frac{2}{\ell_{\text{P}}(\nu, k)} \frac{4\pi Q(\nu)^{n/2}}{1 - Q(\nu)^n},$$
(31)

where  $\ell_{\text{P}}(\nu, k)$  is the elliptic (real) period given by an explicit form  $\ell_{\text{P}}(\nu, k) = 4K(\nu)/k$ , and  $Q(\nu)$  is the nome defined by  $Q(\nu) = \exp(-\pi K'(\nu)/K(\nu))$  with  $K(\nu)$  and  $iK'(\nu) \equiv iK(\sqrt{1-\nu^2})$  being the quarter periods of Jacobian elliptic functions. We compare  $\{M_n^{\text{sn}}(\nu, k), \ell_{\text{P}}(\nu, k)\}$  computed from  $M_{\text{sn}}(z)$  with  $\{M_n^{\text{H}}, \ell_{\text{H}}\}$ . In Table. I, we tabulate the values of potential, elliptic modulus, and harmonic coefficients computed from the SN state  $M_{\text{sn}}$  and those for the HH state at four points introduced above, **A**, **B**, **C**, and **D**. From the table, we see that the energies of these two condensates are nearly degenerate, actually the difference is visible only at the point **D** located in the vicinity of the onset of soliton formation. Nevertheless it is true that the energy for the solitonic SN state is always smaller than that for the HH state. This means that even if we start from the general *Ansatz*  $M_{\text{HH}}(z)$ , the optimized spatial profile of  $M_{\text{HH}}(z)$  approaches that of  $M_{\text{sn}}(z)$ . This fact suggests that the elliptic function gives the absolute ground state. We recognize that the closer to the point  $\eta_2^{\text{I}}$  we get, the more relevant the higher harmonic components become. Near  $\eta_2^{\text{I}}$ ,  $M_{\text{HH}}(z)$  starts to fail to approximate  $M_{\text{sn}}(z)$ ; the departure of  $M_{\text{HH}}(z)$  from  $M_{\text{sn}}(z)$  simply reflects the fact that truncated higher harmonic components ( $n > 5$ ) can no longer be neglected. This is what actually is seen in Fig. 5(b) and (c);  $M_{\text{HH}}(z)$  at points **A** and **C** well approximates  $M_{\text{sn}}(z)$ , while it underestimates both the amplitude and the period at point **D**.

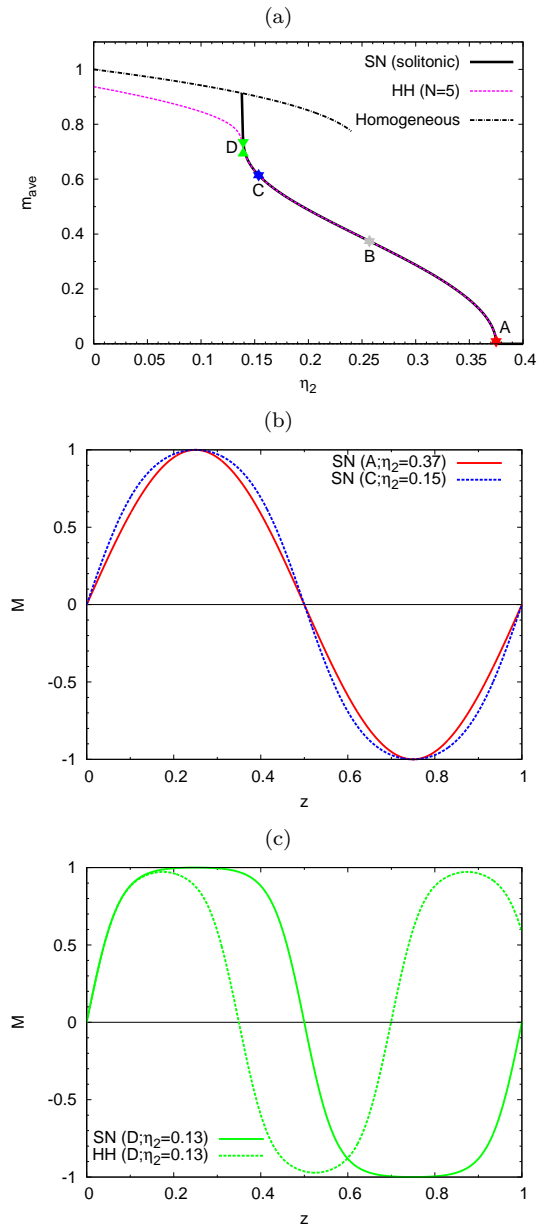


FIG. 5. (color online). **(a)** Spatial profile of the condensate  $M_{\text{sn}}(z)$  at points **A** ( $\eta_2 = 0.3759$ ; solid) and **C** ( $\eta_2 = 0.1536$ ; dashed). For each case, the difference from  $M_{\text{HH}}(z)$  is invisible so it is suppressed from being depicted. The unit of horizontal (vertical) axis  $z$  ( $M$ ) is set to the elliptic period (amplitude) of  $M_{\text{sn}}(z)$ , i.e.,  $\ell_{\text{P}}(\eta_2)$  ( $k(\eta_2)\nu(\eta_2)$ ) at each point. **(b)**  $M_{\text{sn}}$  (solid) and  $M_{\text{HH}}$  (dashed) at point **D** ( $\eta_2 = 0.1389$ ). The scales for  $M$  and the spatial coordinate  $z$  are normalized by the amplitude and the period of  $M_{\text{sn}}(z)$  as in (a).

### C. Multidimensional modulation

We now explore the possibility of realization of higher dimensional crystals favored over the 1D solitonic state. We remark that the EL equation (9) was obtained after the restriction of condensate to one varying in 1D. The

TABLE I. Comparison between  $M_{\text{sn}}(z)$  and  $M_{\text{HH}}(z)$ . The energy densities  $\Omega_{\text{sn}}$  and  $\Omega_{\text{HH}}$ , the values of Fourier strengths  $\{M_1^{\text{H/sn}}, M_3^{\text{H/sn}}, M_5^{\text{H/sn}}\}$ , and modulation periods  $\ell_{\text{H}}$  and  $\ell_{\text{P}}(\nu, k)$  are tabulated at four representative points  $\eta_2 = 0.375, 0.257, 0.154, \text{ and } 0.1393$  which are assigned by the letters **A**, **B**, **C**, and **D**, respectively.

	$\nu$	$\ell_{\text{P}}$	$\ell_{\text{H}}$	$\Omega_{\text{sn}}$	$\Omega_{\text{HH}}$	$M_1^{\text{sn}}$	$M_1^{\text{H}}$	$M_3^{\text{sn}}$	$M_3^{\text{H}}$	$M_5^{\text{sn}}$	$M_5^{\text{H}}$
<b>A</b> ( $\eta_2 = 0.3749$ )	0.009	5.13	5.13	$-9 \times 10^{-10}$	$-9 \times 10^{-10}$	0.0111	0.0111	$6 \times 10^{-8}$	$6 \times 10^{-8}$	$\mathcal{O}(10^{-13})$	$\mathcal{O}(10^{-13})$
<b>B</b> ( $\eta_2 = 0.2569$ )	0.458	5.85	5.85	-0.0038	-0.0038	0.5291	0.5291	0.0077	0.0077	0.0001	0.0001
<b>C</b> ( $\eta_2 = 0.1536$ )	0.821	8.22	8.21	-0.0161	-0.0161	0.8673	0.8665	0.0563	0.0559	0.0039	0.0038
<b>D</b> ( $\eta_2 = 0.1389$ )	0.991	14.98	10.48	-0.0193	-0.0192	1.0672	0.9781	0.1951	0.1077	0.0455	0.0132

original EL equation in 3D is

$$0 = \Delta^2 M(\mathbf{x}) + 3\Delta M(\mathbf{x}) - 10 [M(\nabla M)^2 + M^2 \Delta M] + 6\eta_2 M - 6M^3 + 6M^5, \quad (32)$$

where the operator  $\Delta = \partial_x^2 + \partial_y^2 + \partial_z^2$  is the three-dimensional Laplacian. This is a fourth-order nonlinear *partial* differential equation. The solution space for the partial differential equation is much wider than that for the ordinary differential equation. Therefore it is not trivial that Jacobi's elliptic function stays as the most favorable structure when the restriction to 1D modulations is taken away. Here we do not search for the formal solution, but only try some specific crystals having the simple square or cubic symmetry. In order to demonstrate how the dimensionality of a crystal structure affects the free energy, we concentrate on the LO-type phase which has a simpler form than the elliptic function. We set multi-dimensional LO-type real condensates as

$$\begin{aligned} M_{\text{LO};1\text{D}}(\mathbf{x}) &= \sqrt{2}M_0 \sin(kz), \\ M_{\text{LO};2\text{D}}(\mathbf{x}) &= M_0(\sin(kx) + \sin(ky)), \\ M_{\text{LO};3\text{D}}(\mathbf{x}) &= \sqrt{\frac{2}{3}}M_0(\sin(kx) + \sin(ky) + \sin(kz)). \end{aligned} \quad (33)$$

$M_{\text{LO};2\text{D}}(\mathbf{x})$  is equivalent to the ‘‘egg-carton’’ *Ansatz* in [34]. Each condensate is characterized by two real parameters  $M_0$  and  $q$  whose values are to be determined via minimization of  $\Omega$ . In Fig. 6(a) and (b) we show effective order parameters and free energies. One can see that the energy is an increasing function of the dimensionality. Also it is notable that the critical points at which the transitions from the Wigner to the crystal phases take place are common among all three states. To see this analytically, we expand  $\Omega$  in powers of  $M_0$  as

$$\begin{aligned} \Omega_{\text{LO};1\text{D}} &= \left(\frac{\eta_2}{2} - \frac{3}{16}\right) M_0^2 + \frac{6}{24} M_0^4 + \mathcal{O}(M_0^6), \\ \Omega_{\text{LO};2\text{D}} &= \left(\frac{\eta_2}{2} - \frac{3}{16}\right) M_0^2 + \frac{9}{24} M_0^4 + \mathcal{O}(M_0^6), \\ \Omega_{\text{LO};3\text{D}} &= \left(\frac{\eta_2}{2} - \frac{3}{16}\right) M_0^2 + \frac{10}{24} M_0^4 + \mathcal{O}(M_0^6). \end{aligned} \quad (34)$$

Since the quadratic coefficients take exactly the same form,  $\frac{\eta_2}{2} - \frac{3}{16} \equiv \frac{1}{2}(\eta_2 - \eta_2^{\text{II}})$ , the critical point is shared. On the other hand, from the coefficients of quartic terms, we see that the free energies are on the order of the dimensionality of modulation. The above formulas for energy density can be easily generalized to the case with

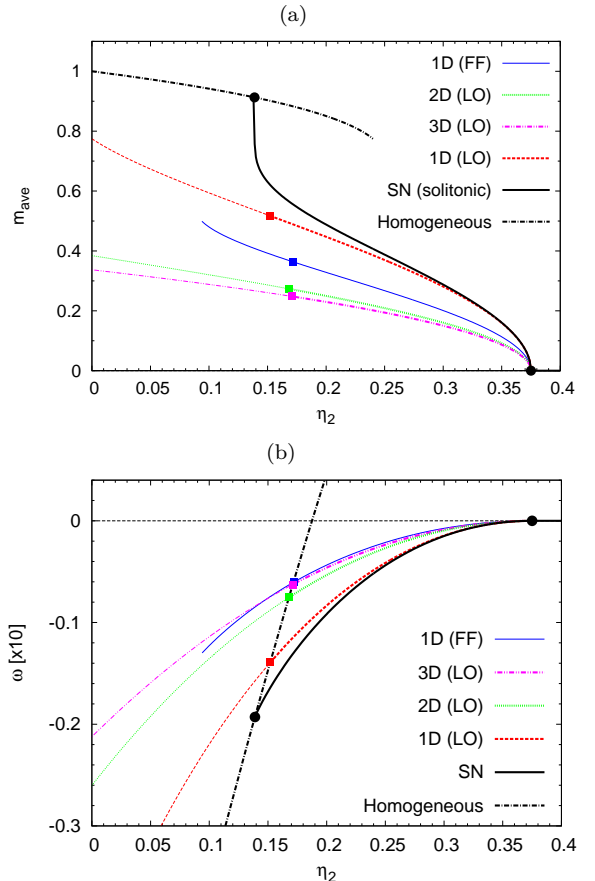


FIG. 6. (color online). **(a)** The effective order parameters for the 1D-LO (dashed, red), 2D-LO (dotted, green), 3D-LO (dot-dot-dashed, magenta), and the solitonic state (solid) as a function of  $\eta_2$ . For comparison, the quantity for the FF phase is also depicted by the thin solid line (blue). **(b)** The thermodynamic potentials as a function of  $\eta_2$ .

the LO condensate in an arbitrary dimension,  $d$ , defined by

$$M_{\text{LO};d\text{D}}(\mathbf{x}) = \sqrt{\frac{2}{d}}M_0(\sin(kx_1) + \dots + \sin(kx_d)), \quad (35)$$

with  $\mathbf{x} = (x_1, x_2, \dots, x_d)$  being the  $d$ -dimensional vector. In this case the thermodynamic potential looks like

$$\begin{aligned} \Omega_{\text{LO};d\text{D}} &= \left(\frac{\eta_2}{2} - \frac{3}{16}\right) M_0^2 + \frac{2d-1}{4d} M_0^4 \\ &\quad + \frac{5(4d^2-16d+11)}{48d^2} M_0^6. \end{aligned} \quad (36)$$

From the dependence of the quartic coefficient on the dimensionality,  $(2d-1)/4d$ , we see that the energy is an increasing function of  $d$  near  $\eta_2 = \eta_2^{\text{II}}$ . In fact, after minimizing over  $M_0$ , the extremal of energy density becomes

$$\Omega_{\text{LO;dD}} = -\left(\frac{\eta_2}{2} - \frac{3}{16}\right)^2 \frac{d}{2d-1} + \mathcal{O}\left(\left(\frac{\eta_2}{2} - \frac{3}{16}\right)^3\right). \quad (37)$$

Note that the higher dimensional LO phases are less favorable than the 1D one, yet they have smaller energies than the 1D-FF (chiral spiral) state.

We remark that the ordering of energies with the dimensionality is not universal, but rather specific to the LO-type. To see this fact, we first *define* the  $d$ -dimensional FF-type complex condensate as

$$M_{\text{FF;dD}}(\mathbf{x}) = \sqrt{\frac{1}{d}} M_0 (e^{ikx_1} + e^{ikx_2} + \dots + e^{ikx_d}). \quad (38)$$

Then after working out similar calculations as in the LO case, we obtain the potential

$$\Omega_{\text{FF;dD}} = \left(\frac{\eta_2}{2} - \frac{3}{16}\right) M_0^2 + \frac{1}{2} M_0^4 - \frac{4d^2+10d-7}{12d^2} M_0^6. \quad (39)$$

In this case we see that the deference first appears at sixth order. Moreover, the coefficient  $(7-10d-4d^2)/(12d^2)$  is no longer a monotonic function of  $d$ ; it has the absolute minimum at  $d = 1.4$ . Above this value, the energy is a monotonically increasing function. Looking up the values  $(4d^2+10d-7)/(12d^2) \cong \{0.55, 0.60, 0.58\}$  for  $d = \{1, 2, 3\}$ , we see that the energy density is on the order of  $\Omega_{\text{FF;2D}} < \Omega_{\text{FF;1D}} < \Omega_{\text{FF;3D}}$ .

We also tried several other, more exotic *Ansätze* for the higher dimensional crystal, including the 2D hexagonal lattices both in the FF type and the LO type, but could not find the structure with energy less than the 1D solitonic state.

#### IV. PHASE STRUCTURE OFF THE TRICRITICAL POINT

We now address the question of how the phase structure changes going away from the tricritical point. As long as we restrict ourselves up to sixth order in the GL potential, the phase structure in the  $[\alpha_2, \text{sgn}(\alpha_4)\alpha_4^2]$  plane is simple such that any phase boundary is expressed by a line starting from the origin. There is no chance for these lines to meet again away from the origin. However this may not be the case in a realistic situation as stated in the Introduction. In this section we thus try to extend the previous analysis going beyond a minimal (sixth order) GL, and see if such nontrivial phase structure indeed shows up off the tricritical point.

General eighth-order terms can be constructed by differentiating the sixth-order terms twice, and collecting terms which are unique up to total derivatives. At order  $\mathcal{O}(\nabla^2)$ , only  $M^4(\nabla M)^2$  comes out, and at order  $\mathcal{O}(\nabla^4)$  three terms  $[(\nabla M)^4, M(\nabla M)^2\Delta M, \text{ and } M^2(\Delta M)^2]$  show up. Finally at order  $\mathcal{O}(\nabla^6)$  only the

term  $(\nabla\Delta M)^2$  is possible. Thus the most general eighth-order terms to be appended to the GL Lagrangian Eq. (2) are collected as

$$\begin{aligned} \delta\omega_8(M(\mathbf{x})) = & \frac{\alpha_8}{8} M^8 + \frac{\alpha_{8b}}{8} M^4(\nabla M)^2 \\ & + \frac{\alpha_{8c}}{8} (\nabla M)^4 + \frac{\alpha_{8d}}{8} M(\nabla M)^2\Delta M \\ & + \frac{\alpha_{8e}}{8} M^2(\Delta M)^2 + \frac{\alpha_{8f}}{8} (\nabla\Delta M)^2. \end{aligned} \quad (40)$$

In NJL-type models, only the quark loops contribute to the GL coefficients. The evaluation of them is tough but straightforward to work out. At the end of the day we arrive at the linear relations (up to total derivatives);

$$(\alpha_{8b}, \alpha_{8c}, \alpha_{8d}, \alpha_{8e}, \alpha_{8f}) = \left(14, -\frac{1}{5}, \frac{18}{5}, \frac{14}{5}, \frac{1}{5}\right) \alpha_8. \quad (41)$$

Thus it is only  $\alpha_8$  that we need to add as a new independent GL parameter.

Here we briefly repeat the dimensional and scaling analyses in this case. Since  $\alpha_8$  has dimension  $\Lambda^{-4}$  and is always positive, we use it for the energy scale. Then by use of  $|\alpha_6|$  we can again tune the magnitude of the sixth- and eighth-order coefficients. To be precise let us introduce the dimensionless GL couplings  $\{\eta_2, \eta_4\}$  and the physical quantities  $\{\tilde{\omega}, m, \tilde{\mathbf{x}}\}$  via

$$\begin{aligned} \alpha_2 &= \eta_2 \left[ \frac{|\alpha_6|^3}{\alpha_8^3} \right], & \alpha_4 &= \eta_4 \left[ \frac{\alpha_6^2}{\alpha_8} \right] \\ \omega &= \tilde{\omega} \left[ \frac{\alpha_6^4}{\alpha_8^4} \right], & M &= m \left[ \frac{|\alpha_6|^{1/2}}{\alpha_8^{1/2}} \right], \\ \mathbf{x} &= \tilde{\mathbf{x}} \left[ \frac{\alpha_8^{1/2}}{|\alpha_6|^{1/2}} \right], & \tilde{\nabla} &= \nabla_{\tilde{\mathbf{x}}}. \end{aligned} \quad (42)$$

Then in these dimensionless bases, we have

$$\begin{aligned} \tilde{\omega} = & \frac{1}{2}\eta_2 m^2 + \frac{1}{4}\eta_4 (m^4 + (\tilde{\nabla} m)^2) \\ & + \frac{\text{sgn}(\alpha_6)}{6} (m^6 + 5m^2(\tilde{\nabla} m)^2 + \frac{1}{2}(\tilde{\Delta} m)^2) \\ & + \frac{1}{8} (m^8 + 14m^4(\tilde{\nabla} m)^2 - \frac{1}{5}(\tilde{\nabla} m)^4 \\ & + \frac{18}{5}m(\tilde{\nabla} m)^2\tilde{\Delta} m + \frac{14}{5}\tilde{m}^2(\tilde{\Delta} m)^2 + \frac{1}{5}(\tilde{\nabla}\tilde{\Delta} m)^2). \end{aligned} \quad (43)$$

In this case, we have two independent dimensionless couplings  $(\eta_2, \eta_4)$ . When  $\alpha_6 > 0$  the limit  $\alpha_8 \rightarrow 0^+$  can be taken, and in this limit the thermodynamics should not depend on  $\alpha_8$  so that the physical quantities depend on  $(\eta_2, \eta_4)$  only through the combination of  $\eta_2/\eta_4^2 = \alpha_2\alpha_6/\alpha_4^2$ . This is the realization of  $(\alpha_2/\alpha_4^2)$  scaling in the absence of eighth-order terms that results in a linear relation between  $\alpha_2$  and  $\alpha_4^2$  at any phase transition. This translates into a linear relation between  $\eta_2$  and  $\eta_4^2$  in the limit of vanishing  $\alpha_8$ . We now expect a nonlinear relation between  $\eta_4^2$  and  $\eta_2$  due to the effect of  $\alpha_8$  by going away from the origin. From now on we throw away tildes on physical quantities, so we should keep in mind that they are dimensionless and properly rescaled quantities.

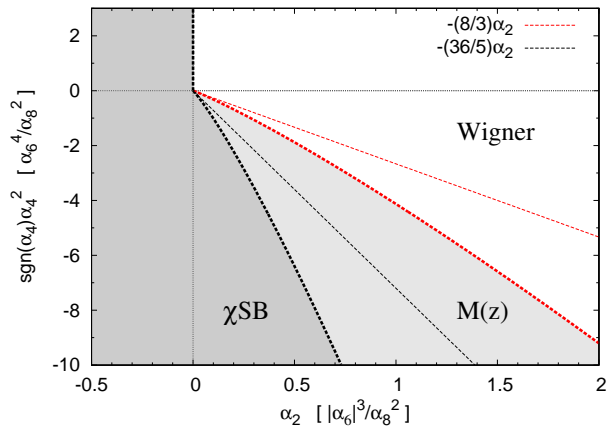


FIG. 7. (color online). Phase diagram for  $\alpha_6 > 0$ : The phase boundaries in the absence of eighth-order terms (see Fig. 3) are also repeated by thin dashed lines, for comparison.

### A. Phase diagram for $\alpha_6 > 0$

We begin the discussion with the case of  $\alpha_6 > 0$  which has a close relation with the previous analyses with  $\alpha_8 = 0$ . The phase diagram for this case is displayed in Fig. 7. The phase boundaries are depicted by dashed lines. All the transitions are of second order. Just for comparison, we also show the phase boundaries obtained for the case  $\alpha_8 = 0$  with two thin dashed lines, which correspond to two lines in Fig. 3. As expected, we see that two critical lines are no longer linear in the plane, which is a simple consequence of the violation of the  $(\eta_2/\eta_4^2)$  scaling. We can derive the analytic formulas for two critical lines. Analyzing the condition of the soliton formation  $\min_{\{M_0, k\}} f(M_0, k, \eta_2, \eta_4) \rightarrow 0^+$  with  $f$  defined by

$$f(M_0, k, \eta_2, \eta_4) \equiv \frac{d\langle \tilde{\omega}(M_{\text{sn}}(z)) \rangle}{d\nu} \Big|_{\nu \rightarrow 1^-}, \quad (44)$$

we easily arrive at the analytical expression for the soliton onset in a closed compact form, which can be expanded in powers of  $\eta_4 < 0$  as

$$\eta_2 = \frac{5}{36}\eta_4^2 + \frac{125}{1512}\eta_4^3 + \frac{3125}{28224}\eta_4^4 + \dots \quad (45)$$

By use of original couplings, this translates into

$$\alpha_2 \alpha_6 = \frac{5}{36}\alpha_4^2 + \frac{125\alpha_8}{1512\alpha_6^2}\alpha_4^3 + \frac{3125\alpha_8^2}{28224\alpha_6^4}\alpha_4^4 + \dots, \quad (46)$$

from which we clearly see that the eighth-order coefficient  $\alpha_8$  is responsible for the nonlinearity between  $\alpha_2$  and  $\alpha_4^2$ . In the same way, we can also derive the compact formula for the critical line dividing the Wigner and inhomogeneous phases. This can be expanded for  $\eta_4 < 0$  as

$$\eta_2 = \frac{3}{8}\eta_4^2 + \frac{27}{160}\eta_4^3 + \frac{2187}{12800}\eta_4^4 + \dots \quad (47)$$

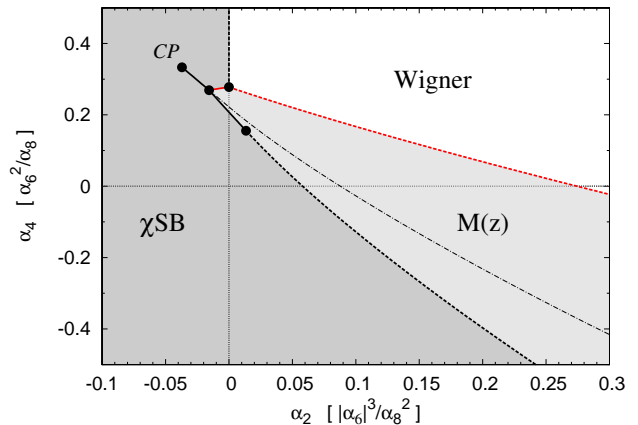
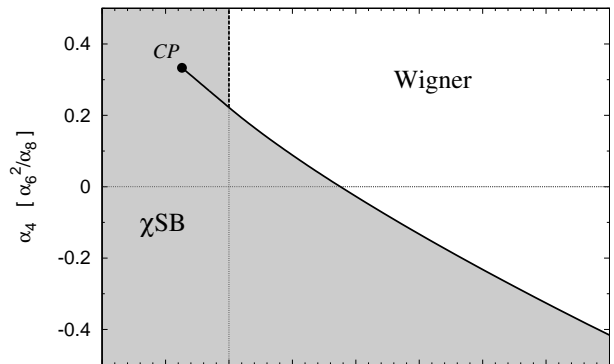


FIG. 8. Phase diagrams for  $\alpha_6 < 0$ : The horizontal (vertical) axis is  $\alpha_2$  ( $\alpha_4$ ) in the appropriate units shown in the parentheses, which is actually equivalent to the dimensionless coupling,  $\eta_2$  ( $\eta_4$ ). The phase diagram obtained with restriction to the homogeneous condensate (upper panel) and that computed without limitation to the homogeneous condensate (lower panel). Solid lines refer to first-order phase transitions, while dashed lines represent the second-order phase transitions.

Again the terms equal to or higher than the cubic term are caused by nonvanishing  $\alpha_8$ . We found that, despite these modifications of two critical lines, the qualitative feature of the phase diagram remains unchanged. In particular, the inhomogeneous phase is still dominated by the one-dimensional modulation characterized by the elliptic function  $M_{\text{sn}}(z) = M_0 \nu \text{sn}(kz, \nu)$  with  $k = M_0$ .

### B. Going to new regime: Phase diagram for $\alpha_6 < 0$

We now have a closer look at the case  $\alpha_6 < 0$  which is not connected in any limits of the previous analysis with  $\alpha_8 = 0$ . In Fig. 8, we show the phase diagrams for  $\alpha_6 < 0$  with and without restriction to the homogeneous condensate.

The upper panel shows the phase diagram computed with restriction to the homogeneous condensate. In this



case, we have first-order chiral restoration even for  $\alpha_4 > 0$  because of negative  $\alpha_6$ . Moreover when  $\alpha_4 > 9/2$  there are two types of  $\chi$ SB phases, one with a larger chiral condensate, and the other with a smaller condensate which we label as the “ $\chi$ SB<sub>2</sub>” phase. The phase transition from the  $\chi$ SB<sub>2</sub> phase to the Wigner phase is second order. On the other hand, the transition between the  $\chi$ SB and the  $\chi$ SB<sub>2</sub> phases is first order. The magnitude of the chiral condensate jumps across the first-order phase transition. The gap between two condensates at the transition decreases with increasing  $\alpha_4$ , and it eventually ends at the critical point marked by  $CP$ . The coordinate of this critical point is found as  $(\eta_2, \eta_4) = (-1/27, 1/3)$ . Accordingly,  $CP$  scales with  $\alpha_6$  as

$$CP : (\alpha_2, \alpha_4) = \left( -\frac{1}{27} \frac{|a_6|^3}{a_8^2}, \frac{1}{3} \frac{a_6^2}{a_8} \right), \quad (48)$$

from which it is clear that point  $CP$  goes to the origin  $(0, 0)$  when  $\alpha_6 \rightarrow 0^-$ ; it smoothly continues to the Lifshitz point in the region  $\alpha_6 > 0$ . At point  $CP$ , the thermodynamic potential takes the following form in the dimensionless units:

$$\tilde{\omega} = -\frac{1}{648} + \frac{1}{8} \left( m^2 - \frac{1}{3} \right)^4. \quad (49)$$

We see that the sixth-order derivative of  $\tilde{\omega}$  with respect to the order parameter  $m$  vanishes at this point. We expect large thermal fluctuation effects in the vicinity of  $CP$ .

The lower panel of the figure shows the phase diagram where the limitation to the homogeneous condensate is taken away. A major part (but not all) of the first-order phase transition splits into two transition lines, and an inhomogeneous phase shows up in between which is dominated again by one-dimensional modulation characterized by the elliptic function. Point  $CP$  remains unaffected by the inclusion of an inhomogeneous condensate.

In addition to  $CP$ , three points show up in the phase diagram. Let us closely investigate these points in the following. In the upper panel of Fig. 9, we present the magnified figure of the phase diagram. First, we notice that the Lifshitz point ( $L$ ) moved to  $\alpha_4 > 0$  from the origin. The situation is the same at the point in which three phases, the homogeneous broken phase, the inhomogeneous phase, and the Wigner phase, meet up. However, it now has the branch of the first-order transition separating the inhomogeneous phase and the homogeneous  $\chi$ SB<sub>2</sub> phase. The exact location of point  $L$  can be found analytically as  $(\eta_2, \eta_4) = (0, 5/18)$  that means

$$L : (\alpha_2, \alpha_4) = \left( 0, \frac{5}{18} \frac{a_6^2}{a_8} \right). \quad (50)$$

Point ( $L$ ) also will become degenerate with the origin as  $\alpha_6 \rightarrow 0^-$ ; it extends to the Lifshitz point in the region  $\alpha_6 > 0$ .

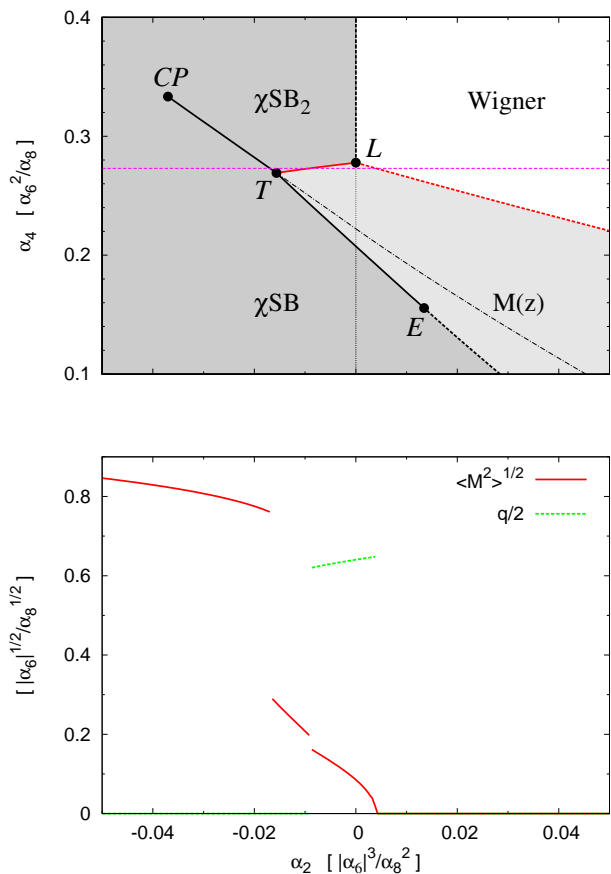


FIG. 9. (color online). (Upper panel) A magnified version of the phase diagram in the  $(\alpha_2, \alpha_4)$  plane for  $\alpha_6 < 0$  in the lower panel of Fig. 8. (Lower panel) The order parameter  $\sqrt{\langle M(z)^2 \rangle}$ , and  $q = 2\pi/\ell_P$  as a function of  $\alpha_2$  along the line  $\alpha_4 = 0.273$  which is displayed in the upper phase diagram by the dashed (magenta) line.

There is also the critical end point ( $E$ ) on the critical line dividing the inhomogeneous phase and the homogeneous broken phase. At this point the second-order phase transition turns into the first-order one. The location of this point can be numerically found as  $(\eta_2, \eta_4) = (0.014, 0.16)$ , that is,

$$E : (\alpha_2, \alpha_4) = \left( 0.014 \frac{|a_6|^3}{a_8^2}, 0.16 \frac{a_6^2}{a_8} \right). \quad (51)$$

The most intriguing point that appears for  $\alpha_6 < 0$  is the triple point denoted by  $T$  in the figure. At this point, three first-order phase transitions meet at once. The location is found numerically as  $(\eta_2, \eta_4) = (-0.016, 0.27)$  which corresponds to

$$T : (\alpha_2, \alpha_4) = \left( -0.016 \frac{|a_6|^3}{a_8^2}, 0.27 \frac{a_6^2}{a_8} \right). \quad (52)$$

Three different forms of the chiral phase compete with each other and coexist at this point. Any dimensionless ratio approaches to some constant when point  $T$  is

approached. We found numerically the following values

$$\begin{aligned} \lim_{(\eta_2, \eta_4) \rightarrow T} \frac{M(\chi\text{SB}_2)}{M(\chi\text{SB})} &= 0.369 \dots, \\ \lim_{(\eta_2, \eta_4) \rightarrow T} \frac{\sqrt{\langle M(z)^2 \rangle}}{M(\chi\text{SB})} &= 0.308 \dots, \\ \lim_{(\eta_2, \eta_4) \rightarrow T} \frac{q}{\sqrt{\langle M(z)^2 \rangle}} &= 5.001 \dots, \end{aligned} \quad (53)$$

where  $q = 2\pi/\ell_P$  with  $\ell_P$  being the elliptic period. All these ratios are universal in the sense that they do not depend on any of the GL couplings. Thus we would say these ratios are associated with the triple point ( $T$ ) itself. In other words, these values characterize the point ( $T$ ). Therefore the values obtained here are model independent and should be shared by all theories which allow the existence of such triple point.

All four points,  $CP$ ,  $T$ ,  $L$ , and  $E$ , discussed above get shrunk to the origin when the limit  $\alpha_6 \rightarrow 0^-$  is taken, and they continue to the Lifshitz point in the region  $\alpha_6 > 0$ .

In the lower panel of Fig. 9, we show the effective order parameter  $\sqrt{\langle M(z)^2 \rangle}$ , and  $q$  as a function of  $\alpha_2$  along the section  $\eta_4 = 0.273$  which is depicted by a horizontal dashed (magenta) line in the phase diagram displayed in the upper panel. We see that the chiral restoration in this case proceeds via three steps: first from the  $\chi\text{SB}$  to the  $\chi\text{SB}_2$  phase, second from the  $\chi\text{SB}_2$  to the inhomogeneous phase, and last from the inhomogeneous phase to the Wigner phase through second-order phase transition.

### C. How does the GL map onto the $(\mu, T)$ phase diagram?

The microscopic evaluation of GL couplings within the NJL model can be summarized in the form [10]

$$\alpha_{2n} = \frac{\delta_{n,1}}{2G} + 4N_c N_f T \sum_m \int \frac{d\mathbf{p}}{(2\pi)^3} \frac{1}{(i\omega_m + \mu)^2 - p^2}{}^n, \quad (54)$$

where  $\omega_m = \pi T(2m + 1)$  is the fermionic Matsubara frequency. The summation over the frequency can be done, resulting in the following expressions for  $\alpha_2$  and  $\alpha_4$

$$\alpha_2 = \frac{1}{2G} - 4N_c N_f \int \frac{d\mathbf{p}}{(2\pi)^3} \frac{1 - f_F(p-\mu) - f_F(p+\mu)}{2p}, \quad (55a)$$

$$\begin{aligned} \alpha_4 &= N_c N_f \int \frac{d\mathbf{p}}{(2\pi)^3} \frac{1 - f_F(p-\mu) - f_F(p+\mu)}{p^3} \\ &+ N_c N_f \int \frac{d\mathbf{p}}{(2\pi)^3} \frac{f'_F(p-\mu) + f'_F(p+\mu)}{p^2}. \end{aligned} \quad (55b)$$

We can derive similar expressions for higher order coefficients. The momentum integral in  $\alpha_2$  ( $\alpha_4$ ) has quadratic (logarithmic) divergence so that we need a cut-off  $\Lambda$ . As a consequence, their functional forms become  $\alpha_2 = \Lambda^2 f_1(\mu/\Lambda, T/\Lambda, g)$  and  $\alpha_4 = f_2(\mu/\Lambda, T/\Lambda)$  with  $g \equiv G\Lambda^2$  as the dimensionless NJL coupling and  $\{f_n\}$  being some dimensionless functions. Higher order coefficients,  $\alpha_{2n}$  ( $n \geq 3$ ), no longer have the UV divergence so that their functional forms can be summarized

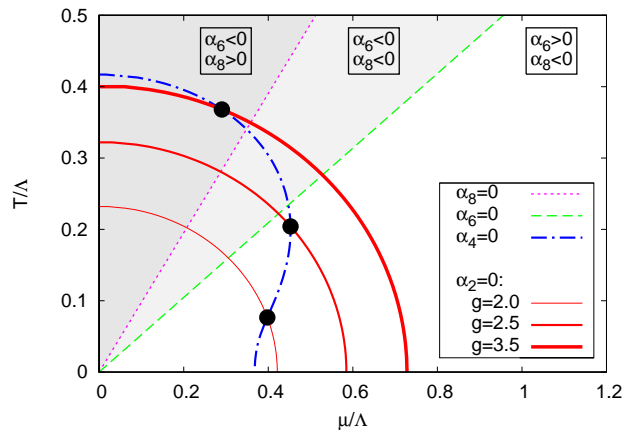


FIG. 10. (color online). Mapping of the conditions of vanishing GL coefficients to the  $(\mu, T)$ -phase space. Solid (red) lines correspond to  $\alpha_2 = 0$  for several different values of the NJL coupling;  $g = G\Lambda^2$ , 2.0 (light), 2.5 (medium), and 3.5 (heavy). The dot-dashed (blue) line presents the condition  $\alpha_2 = 0$  and  $\alpha_4 = 0$ . The intersection of the lines,  $\alpha_2 = 0$  and  $\alpha_4 = 0$ , provides the candidate of the critical point. Area shadings are made according to the signs of  $\alpha_6$  and  $\alpha_8$ .

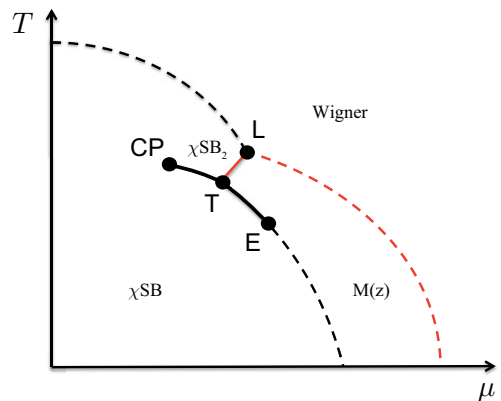


FIG. 11. Conjectured, schematic phase diagram. The Lifshitz point splits into four critical points: the Lifshitz point, the critical point, the end point, and the triple point, labeled by  $L$ ,  $CP$ ,  $E$ , and  $T$ , respectively.

as  $\alpha_{2n}(\mu, T) = f_n(\mu/T)/\mu^{2(n-2)}$ .  $f_1$  ( $f_2$ ) is a function having three (two) arguments, while  $f_n$  for ( $n \geq 3$ ) has only a single argument,  $\mu/T$ . Thus the condition of vanishing  $\alpha_{2n}$  for  $n \geq 3$  turns into a straight line in the  $(\mu, T)$  plane if  $f_n(x) = 0$  has a solution for  $x \geq 0$ .

It is easy to evaluate the vanishing conditions of  $\alpha_{2,4,6,8}$ , and the results are depicted in the  $(\mu/\Lambda, T/\Lambda)$  plane in Fig. 10. Solid (red) curves show the vanishing of  $\alpha_2$  for  $g = 2.0$  (light),  $g = 2.5$  (medium), and  $g = 3.5$  (heavy), respectively. The dot-dashed (blue) curve represents the vanishing of  $\alpha_4$ . The intersection of these two curves, where  $\alpha_2 = \alpha_4 = 0$ , presents the candidate of the location of the critical point, in the absence of inhomogeneous

geneous condensates. We see that the location shifts to higher temperatures with increasing the strength of the NJL coupling,  $g$ , while its  $\mu$  coordinate shows nonmonotonic dependence on  $g$ .

The long-dashed (green) line and the dashed (magenta) line show the lines for vanishing  $\alpha_6$  and  $\alpha_8$ , respectively. Accordingly, the condition ( $\alpha_8 > 0$ ,  $\alpha_6 < 0$ ) is realized in the shaded area, while  $\alpha_8$  changes its sign in the lightly shaded area where ( $\alpha_8 < 0$ ,  $\alpha_6 < 0$ ) is satisfied. The region without shading corresponds to ( $\alpha_6 > 0$ ,  $\alpha_8 < 0$ ). The present analysis suggests that if the “would-be” critical point is located in the shaded area, this point may split to the four independent points,  $CP$ ,  $T$ ,  $L$ , and  $E$  discussed in the previous section. If this is the case, the corresponding  $(\mu, T)$ -phase diagram might become the one schematically depicted in Fig. 11

We remark that this interesting situation is realized for very large values of the NJL coupling. The NJL coupling empirically has taken ranges from  $g \cong 1.8$  to  $g \cong 2.5$  depending on the presence/absence of the 't Hooft coupling [2, 5, 41, 42]. Then it would be unlikely to have the triple point in the standard version of the NJL model. It would be interesting to investigate if the situation could be realized in the extended version of the NJL models such as one incorporated with the Polyakov-loop [43–47], the other type interactions, the diquark degrees of freedom, etc.

## V. SUMMARY

We have made an extensive analysis on inhomogeneous chiral condensates using the Ginzburg-Landau approach. We first reviewed the work by Nickel [10] with special emphasis put on the mechanism of the formation of a chiral domain wall. We have also discussed singular behaviors of the thermodynamic quantities in the vicinity of soliton formation.

We then analyzed the most general condensate of the 1D modulation,  $M_{\text{HH}}(z)$  expanded in harmonics. We confirmed that  $M_{\text{HH}}$  seems to converge to the solitonic state characterized by Jacobi’s elliptic function by increasing the number of harmonics. It well approximates the solitonic condensate except for in the vicinity of a domain wall onset, already at the level of truncation with the first few harmonics. This strongly suggests that the elliptical solitonic state is the most favorable structure within 1D modulations.

We then explored the possibility of realization of multidimensional chiral crystals. Taking several *Ansätze* for multidimensional structures, we compared free energies. We have shown that, in the case of real condensates of the LO-type, the free energy density is an increasing function of the dimensionality of modulation  $d$ . On the other hand, it has been confirmed that the energy takes a minimum for  $d = 2$  in the case of complex condensate of the FF-type. We derived analytic expressions for the effective potentials, both for the real and complex con-

densates forming a simple square and cubic lattices. The order of energy was correctly understood based on the GL expansion near the critical point.

Since we have restricted our analyses to simple lattice structures, the quest for such crystal structures remains the subject of continuing interest. In particular, because simple 1D structures are known to be unstable against the thermal fluctuation [48], we should clarify how the 1D structure could be stabilized if we really have no suitable multidimensional structure.

We have investigated the phase structure away from the tricritical point by extending the previous GL functional to one expanded on the order parameter and its spatial derivative up to eighth order. With this extension, we analyzed phase structures both for  $\alpha_6 > 0$  and  $\alpha_6 < 0$ . For  $\alpha_6 > 0$ , we have seen that two critical lines enclosing the inhomogeneous phase change their slopes in the  $[\alpha_2, \text{sgn}(\alpha_4)\alpha_4^2]$  plane by going away from the Lifshitz point. This is a natural consequence of including the eighth-order terms. We have derived the analytical expressions for the two critical curves. However no new phase structure was found to appear even largely departing from the Lifshitz point.

On the other hand, once  $\alpha_6$  changes its sign to negative,  $\alpha_6 < 0$ , several qualitative changes appear immediately in the  $(\alpha_2, \alpha_4)$ -phase diagram. We have seen that the Lifshitz point located at the origin for  $\alpha_6 > 0$  splits into four critical points; these are the critical point ( $CP$ ), the triple point ( $T$ ), the end point ( $E$ ), and the new Lifshitz point ( $L$ ), which has a branch of the first-order phase transition. The distances among these points grow with increasing the magnitude of  $|\alpha_6|$ . There are two kinds of homogeneously symmetry-broken phases in this case: one with a larger chiral condensate  $\chi\text{SB}$ , and the other with a smaller chiral condensate which we label by  $\chi\text{SB}_2$ . They are separated by a first-order phase transition extending from the triple point ( $T$ ) to the critical point ( $CP$ ) at which the phase transition terminates. Most intriguing is the emergence of the triple point ( $T$ ) where three different forms of the chiral phase,  $\chi\text{SB}$ ,  $\chi\text{SB}_2$  and the inhomogeneous (solitonic) phase, are present. Any dimensionless ratios of physical quantities approach some specific values when the triple point ( $T$ ) is approached. These values are universal, model independent, being associated with the triple point itself. We have extracted numerically the universal ratios associated with the triple point ( $T$ ).

There are several possible extensions of the current work. We have restricted our analyses to the chiral limit. It is straightforward to extend our work so as to include the effect of a finite current quark mass along the line of [30]. It may also be interesting to try the most general complex condensate, the twisted chiral crystal [31], even though a simple chiral spiral condensate of the FF type turned out to be the most favorable structure within a 1D-NJL model [32]. Also the interplay between the chiral condensate and color superconductivity is of particular interest since it was shown that there is an entanglement

between them via the axial anomaly in QCD [49]. Its effects have been proven to be so drastic that it brings a rich phase structure near the critical point [49–52]. A more interesting, but challenging issue is the first principle determination of the Ginzburg-Landau coefficients with the lattice QCD. Extension of the present work in these directions deserves future work.

### ACKNOWLEDGMENTS

T. Brauner, Y. Hidaka, Y. Iwata, K. Kamikado, T. Kojo, A. Ohnishi, D. Rischke, M. Ruggieri and

J. Wambach are acknowledged for their interests in this work and several suggestive comments. We thank all the members of the theoretical quark/hadron group at Tokyo University of Science for useful conversations.

- 
- [1] J. C. Collins and M. Perry, *Phys. Rev. Lett.* **34**, 1353 (1975).
- [2] T. Hatsuda and T. Kunihiro, *Phys. Rept.* **247**, 221 (1994), arXiv:hep-ph/9401310 [hep-ph].
- [3] Y. Nambu and G. Jona-Lasinio, *Phys. Rev.* **124**, 246 (1961).
- [4] H. Fukaya *et al.* (JLQCD and TWQCD collaborations), *Phys. Rev.* **D83**, 074501 (2011), arXiv:1012.4052 [hep-lat].
- [5] S. Klevansky, *Rev. Mod. Phys.* **64**, 649 (1992).
- [6] D. V. Deryagin, D. Y. Grigoriev, and V. A. Rubakov, *Int. J. Mod. Phys.* **A7**, 659 (1992).
- [7] E. Shuster and D. T. Son, *Nucl. Phys.* **B573**, 434 (2000), arXiv:hep-ph/9905448.
- [8] M. Sadzikowski and W. Broniowski, *Phys. Lett.* **B488**, 63 (2000), arXiv:hep-ph/0003282.
- [9] E. Nakano and T. Tatsumi, *Phys. Rev.* **D71**, 114006 (2005), arXiv:hep-ph/0411350.
- [10] D. Nickel, *Phys. Rev. Lett.* **103**, 072301 (2009), arXiv:0902.1778 [hep-ph]; *Phys. Rev.* **D80**, 074025 (2009), arXiv:0906.5295 [hep-ph].
- [11] P. Fulde and R. A. Ferrell, *Phys. Rev.* **135**, A550 (1964).
- [12] A. Larkin and Y. Ovchinnikov, *Zh. Eksp. Teor. Fiz.* **47**, 1136 (1964); *Sov. Phys. JETP* **20**, 762 (1965).
- [13] S. Carignano, D. Nickel, and M. Buballa, *Phys. Rev.* **D82**, 054009 (2010), arXiv:1007.1397 [hep-ph].
- [14] A. Buzdin, Y. Matsuda, and T. Shibauchi, *Euro. Lett.* **80**, 67004 (2007).
- [15] T. Kunihiro and R. Tamagaki, *Prog. Theor. Phys.* **61**, 1107 (1979); T. Kunihiro, T. Takatsuka, and R. Tamagaki, **73**, 683 (1985).
- [16] D. Ebert, N. Gubina, K. Klimenko, S. Kurbanov, and V. Zhukovsky, *Phys. Rev.* **D84**, 025004 (2011), arXiv:1102.4079 [hep-ph].
- [17] M. G. Alford, J. A. Bowers, and K. Rajagopal, *Phys. Rev.* **D63**, 074016 (2001), arXiv:hep-ph/0008208 [hep-ph].
- [18] J. A. Bowers, J. Kundu, K. Rajagopal, and E. Shuster, *Phys. Rev.* **D64**, 014024 (2001), arXiv:hep-ph/0101067 [hep-ph].
- [19] A. K. Leibovich, K. Rajagopal, and E. Shuster, *Phys. Rev.* **D64**, 094005 (2001), arXiv:hep-ph/0104073 [hep-ph].
- [20] R. Casalbuoni and G. Nardulli, *Rev. Mod. Phys.* **76**, 263 (2004), arXiv:hep-ph/0305069; R. Casalbuoni, M. Ciminale, M. Mannarelli, G. Nardulli, M. Ruggieri, *et al.*, *Phys. Rev.* **D70**, 054004 (2004), arXiv:hep-ph/0404090 [hep-ph]; R. Casalbuoni, R. Gatto, N. Ippolito, G. Nardulli, and M. Ruggieri, *Phys. Lett.* **B627**, 89 (2005), arXiv:hep-ph/0507247.
- [21] D. Nickel and M. Buballa, *Phys. Rev.* **D79**, 054009 (2009), arXiv:0811.2400 [hep-ph].
- [22] G. Basar, G. V. Dunne, and D. E. Kharzeev, *Phys. Rev. Lett.* **104**, 232301 (2010), arXiv:1003.3464 [hep-ph].
- [23] B. Bringoltz, *Phys. Rev.* **D79**, 125006 (2009), arXiv:0901.4035 [hep-lat].
- [24] T. Kojo, Y. Hidaka, L. McLerran, and R. D. Pisarski, *Nucl. Phys.* **A843**, 37 (2010), arXiv:0912.3800 [hep-ph].
- [25] T. Kojo, R. D. Pisarski, and A. M. Tsvelik, *Phys. Rev.* **D82**, 074015 (2010), arXiv:1007.0248 [hep-ph].
- [26] T. Kojo, Y. Hidaka, K. Fukushima, L. McLerran, and R. D. Pisarski, *Nucl. Phys.* **A875**, 94 (2012), arXiv:1107.2124 [hep-ph].
- [27] V. Schon and M. Thies, (2000), arXiv:hep-th/0008175.
- [28] O. Schnetz, M. Thies, and K. Urlichs, *Annals Phys.* **314**, 425 (2004), arXiv:hep-th/0402014 [hep-th].
- [29] O. Schnetz, M. Thies, and K. Urlichs, *Annals Phys.* **321**, 2604 (2006), arXiv:hep-th/0511206 [hep-th].
- [30] C. Boehmer, M. Thies, and K. Urlichs, *Phys. Rev.* **D75**, 105017 (2007), arXiv:hep-th/0702201.
- [31] G. Basar and G. V. Dunne, *Phys. Rev. Lett.* **100**, 200404 (2008), arXiv:0803.1501 [hep-th]; *Phys. Rev.* **D78**, 065022 (2008), arXiv:0806.2659 [hep-th].
- [32] G. Basar, G. V. Dunne, and M. Thies, *Phys. Rev.* **D79**, 105012 (2009), arXiv:0903.1868 [hep-th].
- [33] M. Asakawa and K. Yazaki, *Nucl. Phys.* **A504**, 668 (1989).
- [34] S. Carignano and M. Buballa, (2011), arXiv:1111.4400 [hep-ph].
- [35] R. Combescot and C. Mora, *Phys. Rev.* **B71**, 144517 (2005).
- [36] S. Matsuo, S. Higashitani, Y. Nagato, and K. Nagai, *J. Phys. Soc. Jpn.* **67**, 280 (1998).
- [37] A. I. Buzdin and H. Kachkachi, *Phys. Lett.* **A225**, 341 (1997).
- [38] M. Houzet, Y. Meurdesoif, O. Coste, and A. Buzdin, *Physica* **C316**, 89 (1999).
- [39] N. Yoshida and S.-K. Yip, *Phys. Rev.* **A75**, 063601 (2007).
- [40] A. Bulgac and M. M. Forbes, *Phys. Rev. Lett.* **101**,



- 215301 (2008), arXiv:0804.3364 [cond-mat.supr-con].
- [41] M. F. Lutz, S. Klimt, and W. Weise, Nucl. Phys. **A542**, 521 (1992).
- [42] M. Buballa, Phys. Rept. **407**, 205 (2005), arXiv:hep-ph/0402234 [hep-ph].
- [43] K. Fukushima, Phys. Lett. **B591**, 277 (2004), arXiv:hep-ph/0310121.
- [44] C. Ratti, M. A. Thaler, and W. Weise, Phys. Rev. **D73**, 014019 (2006), arXiv:hep-ph/0506234.
- [45] H. Abuki, M. Ciminale, R. Gatto, N. Ippolito, G. Nardulli, and M. Ruggieri, Phys. Rev. **D78**, 014002 (2008), arXiv:0801.4254 [hep-ph].
- [46] H. Abuki, M. Ciminale, R. Gatto, G. Nardulli, and M. Ruggieri, Phys. Rev. **D77**, 074018 (2008), arXiv:0802.2396 [hep-ph]; H. Abuki, R. Anglani, R. Gatto, G. Nardulli, and M. Ruggieri, **D78**, 034034 (2008), arXiv:0805.1509 [hep-ph].
- [47] H. Abuki and K. Fukushima, Phys. Lett. **B676**, 57 (2009), arXiv:0901.4821 [hep-ph].
- [48] G. Baym, B. Friman, and G. Grinstein, Nucl. Phys. **B210**, 193 (1982).
- [49] T. Hatsuda, M. Tachibana, N. Yamamoto, and G. Baym, Phys. Rev. Lett. **97**, 122001 (2006), arXiv:hep-ph/0605018.
- [50] N. Yamamoto, T. Hatsuda, M. Tachibana, and G. Baym, J. Phys. **G34**, S635 (2007), arXiv:hep-ph/0701191.
- [51] H. Abuki, G. Baym, T. Hatsuda, and N. Yamamoto, Phys. Rev. **D81**, 125010 (2010), arXiv:1003.0408 [hep-ph].
- [52] H. Basler and M. Buballa, Phys. Rev. **D82**, 094004 (2010), arXiv:1007.5198 [hep-ph].